

Contents lists available at ScienceDirect

International Journal of Non-Linear Mechanics

journal homepage: www.elsevier.com/locate/nlm



Strong geometric softening–hardening nonlinearities in an oscillator composed of linear stiffness and damping elements



Alireza Mojahed a,*, Keegan Moore a, Lawrence A. Bergman b, Alexander F. Vakakis a

- ^a Department of Mechanical Science and Engineering, University of Illinois, Urbana, IL 61801, United States
- ^b Department of Aerospace Engineering, University of Illinois, Urbana, IL 61801, United States

ARTICLE INFO

Keywords:
Geometric nonlinearity
Hardening/softening nonlinearity
Nonlinear damping
Complexification-averaging method

ABSTRACT

A single-degree-of-freedom (SDOF) oscillator grounded through a linear spring in parallel with a linear viscous damper, and two inclined pairs of linear spring-damper elements forming an initial angle of inclination, ϕ_0 , with the horizontal at equilibrium, is considered. It is assumed that there is no pre-compression in any element. An impulsive excitation is applied to this system, and it is shown that, depending on the system parameters, the intensity of the applied impulse and the initial angle of inclination, there are strong stiffness and damping nonlinearities in the transient response induced solely due to geometric effects; these strong nonlinearities occur even though all elastic and dissipative elements of the system are governed by linear constitutive laws. Preliminary numerical simulations indicate that in different regimes of the dynamics the geometric nonlinearities are of hardening, hardening-softening or softening type. An analytical study is then performed to reveal two bifurcations in the dynamics with respect to the initial angle of inclination and detect the critical energy beyond which the nonlinearity changes from hardening to softening. Another effect of the initial angle of inclination is that it "slows" the decay rate of the transient response. To investigate this effect analytically, the complexification-averaging method is applied to an approximate (truncated) equation of motion, to show that, for non-zero initial angle of inclination, the time-scale of the slow dynamics of the system is directly related to the initial angle of inclination. An experimental study is then performed to verify the analytical and numerical predictions. The experimental system consists of a beam clamped at one of its ends and grounded by the inclined linear spring element at its other end. System identification is performed to identify the (linear) modal properties of the beam and detect the linear stiffness and viscous damping characteristics of the inclined spring. The experiments are performed for several different initial angles and initial conditions in order to obtain sufficient measured time series to be able to verify the theoretical predictions. The experimental results confirm the theoretical findings. This study highlights the strong hardening-softening stiffness and damping nonlinearities that may be induced by geometric (and/or kinematic) effects in oscillating systems composed of otherwise linear stiffness and damping elements.

1. Introduction

Despite the extensive current literature on the design of passive vibration suppression systems, this area still attracts the attention of scientists and engineers [1,2]. Examples of areas of current interest can be found in civil engineering, e.g., in the design of vibration mitigation systems that reduce the vibration transmitted to structures due to seismic excitations; and in mechanical engineering, e.g., in mitigating flow-induced vibrations resulting from flow-structure interaction, and in suppression of dynamic instabilities in rotating machineries such as engines, motors, pumps, and fans. Numerous passive mechanisms have been considered as vibration mitigation mechanisms, both with linear and nonlinear dynamical characteristics. Examples of linear vibration mitigation systems are tuned vibration neutralizers (TVNs),

tuned vibration absorbers (TVAs) and tuned mass dampers (TMDs) [3–8]. As for nonlinear vibration isolators, one can mention nonlinear energy sinks (NESs) [9–12], negative-stiffness vibration isolators, and magnetic vibration isolators [13–18]. Focusing on nonlinear designs, nonlinear vibration isolators such as NESs are designed to dissipate the unwanted vibrational energy through resonance captures in an irreversible manner, i.e., by means of targeted energy transfer (TET). In the case of vibration isolators with negative stiffness, however, the unwanted vibrational energy is dissipated by intentionally scattering it to higher frequencies through excitation of higher harmonics or by means of resonance captures between super-harmonics and structural modes of the main structure [12]. For instance, Carella et al. introduced and studied a quasi-zero-stiffness passive nonlinear vibration

https://doi.org/10.1016/j.ijnonlinmec.2018.09.004

^{*} Corresponding author.

E-mail address: mojahed2@illinois.edu (A. Mojahed).

isolator [14,19]; their proposed vibration isolator could have negative stiffness depending on the geometric parameters of the system. Also, Sarlis et al. designed and experimentally tested a nonlinear vibration isolator system to protect structures from seismic activity [20]; the nonlinearity in that system was due to geometric effects of the isolator, again yielding negative stiffness characteristics.

In this work we consider a nonlinear oscillator with geometricallyinduced stiffness and damping nonlinearities and examine its efficacy as a vibration isolator. Due to their simplicity to implement, it is common to utilize geometric and kinematic effects to realize nonlinearities in mechanical systems composed of linear elastic and/or dissipative elements. Carella et al. introduced the nonlinearity in their proposed system through the specific configuration of the nonlinear attachment. In their study, the geometric effect introduced negative stiffness to the system [14,19], and they were able to propose a vibration isolator which was more efficient than the corresponding linear one. Moreover, to enhance the efficiency of their proposed vibration isolation mechanism compared to typical linear vibration isolators, Carella et al. proposed an alternative nonlinear vibration isolator based on geometric nonlinearity [21]. In that mechanism a system with high static stiffness and low dynamic stiffness was introduced with the aim to minimize the transmitted force through geometric effects. A more in-depth study of the effects of geometric nonlinearity on the dynamics of a two DOF system was presented in the work by Andersen et al. [22]. The system studied in that work consisted of an elastically grounded linear oscillator and an NES attached to it in which the nonlinearity was realized through geometrical effects. A new feature of that work was that the geometry of the motion introduced a combination of stiffness and damping nonlinearities which affected significantly the response. In particular, it was shown that geometrical nonlinear damping could have unexpected effects on the dynamics, including multi-frequency instabilities; in linear settings such damping-induced instabilities can be induced only in gyroscopic systems, and, typically, the effect of linear damping is parasitic, i.e., it yields a decay of the free response of the damped system. Yet, the results reported in [22] showed for the first time that geometrically nonlinear damping can have non-parasitic dynamical effects, e.g., yielding free responses that do not monotonically decay with time. Moreover, Cho et al. showed that through geometric effects it is possible to achieve transitions from hardening to softening nonlinear stiffness behavior in micro/nanomechanical resonators by properly tuning the system parameters [23]. In addition, in order to improve the performance of microelectromechanical systems (MEMS) and overcome the limitations of linear MEMS, Asadi et al. incorporated geometric nonlinearity into their system [24]. They were able to induce a drastic transformation between the axial and bending stiffnesses of the Si and polymer components of their MEMS device by changing the geometric properties.

The principal aim of this work is to study theoretically and validate experimentally a new way to induce strong and tunable stiffness and damping nonlinearities in an impulsively forced oscillator through purely geometric effects. By this we mean that, although the oscillator is composed of stiffness and damping elements obeying linear constitutive laws, the effects of geometry yield strong nonlinearities, which depending on the energy and the system parameters can be hardening, softening, or a combination of both (in different regimes of the same response). The oscillator is grounded by means of a linear spring-viscous damper pair in parallel, as well as two inclined spring-damper pairs forming an initial angle of inclination, ϕ_0 , with the horizontal at equilibrium. The transient dynamics of this system are examined numerically by direct numerical integration of the governing equations of motion, and analytically by introducing slow-fast partitions of the transient dynamics and following a complexification-averaging method. This enables us to gain predictive capability of the design of the geometric nonlinearities in this system, and to gain a good physical understanding of the effects on the transient dynamics that are induced by these strong nonlinearities. In addition, we provide an experimental validation of the theoretical findings by

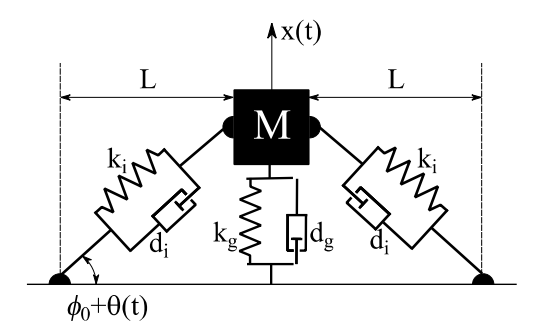


Fig. 1. Configuration of the nonlinear oscillator.

fabricating, characterizing and testing a specially built experimental fixture. The experimental results confirm the theoretical predictions and highlight the important local nonlinear effects that geometry can have on the global dynamics of a mechanical system comprised of otherwise linear components.

2. Formulation of the model

The system under consideration is a nonlinear single-degree-of-freedom (SDOF) system of mass, M, which is grounded via a linear spring with stiffness, k_g , in parallel to a linear viscous damper with damping coefficient, d_g , and two inclined parallel spring–dashpot elements with linear nominal stiffness and damping coefficient, k_i and d_i , respectively. The inclined elements have an initial angle of inclination, ϕ_0 , with the ground while the system is at rest; moreover, it is assumed that the inclined springs and dampers are unstretched at the equilibrium position of the system. The initial angle of inclination is the basic geometric parameter that introduces stiffness and damping nonlinearity to the system. The configuration of the system is shown in Fig. 1.

Assuming that the impulse $F(t) = F\delta(t)$ is applied to the system while at rest, the governing equation of motion and the initial conditions at t=0+ are given by,

$$\begin{split} M \ddot{x} + d_g \dot{x} + k_g x + 2F_i \sin(\phi_0 + \theta) &= 0, \\ x(0+) &= 0, \dot{x}(0+) = F/M \equiv I_0, \end{split} \tag{1a}$$

where F_i is the combined force exerted by each inclined spring–damper pair, x(t) is the vertical displacement of the oscillator from equilibrium, and $\theta(t)$ the corresponding increment of the angle of inclination. Using simple geometric arguments, the total vertical component of the force exerted by each inclined pair to the mass is determined to be

$$\begin{split} F_{i}\sin(\phi_{0}+\theta) &= \left[k_{i}\Delta u + d_{i}\frac{d(\Delta u)}{dt}\right]\sin(\phi_{0}+\theta) = \\ k_{i}\left[y - \left(L\sec\phi_{0}\right)y/\sqrt{L^{2}+y^{2}}\right] + d_{i}\dot{y}y^{2}/\left(L^{2}+y^{2}\right) \end{split} \tag{1b}$$

where $\Delta u = \sqrt{\left[L \sec \phi_0\right]^2 + x^2 + 2xL \tan \phi_0} - L \sec \phi_0$ and $y = x + L \tan \phi_0$. Combining all terms in (1) we may re-write these systems of equations

$$M \ddot{x} + F_s + F_d = 0,$$

 $x(0+) = 0, \dot{x}(0+) = F/M \equiv I_0,$ (2a)

where F_s and F_d are the combined forces exerted in the vertical direction by the stiffness and damping elements of the system, respectively, and given by

$$F_{s} = \left[k_{g} + 2k_{i} \left[1 - \left(L \sec \phi_{0} \right) / \sqrt{L^{2} + y^{2}} \right] \right] y - k_{g} L \tan \phi_{0}$$

$$F_{d} = \left[d_{g} + 2d_{i} y^{2} / \left(L^{2} + y^{2} \right) \right] \dot{y}$$
(2b)

It is clear that the geometry of the motion introduces strongly nonlinear effects in the dynamics, despite the fact that all stiffness and damping elements of the oscillator obey linear constitutive laws. Hence,

Table 1System parameters used in the numerical simulations.

Parameter	Value
M [kg]	0.1
$k_i [N/m]$	20 000
$k_{\rm g}$ [N/m]	240
d_i [Ns/m]	0.25
$d_{\rm g}$ [Ns/m]	0.5
L [°] [m]	0.05

before we analyze the transient dynamics of this system it is necessary to gain some more insight into the geometric effects on the stiffness and damping forces that result from the variation of the initial angle of inclination, ϕ_0 . Specifically, it is of interest to consider the type of nonlinearity (hardening or softening) that is obtained depending on the selection of the angle ϕ_0 .

To this end, we express the Eqs. (2a), (2b) in normalized form as,

$$\begin{split} \hat{x}'' + f_s + f_d &= 0, \\ f_s &= \frac{\hat{y} + 2\beta \hat{y} \left(1 - \frac{\sec \phi_0}{\sqrt{1 + \hat{y}^2}}\right) - \tan \phi_0}{1 + 2\beta \sin^2 \phi_0}, \quad f_d &= \frac{d_i \left[\mu + 2\hat{y}^2 / (1 + \hat{y}^2)\right] \hat{y}'}{k_g + 2k_i \sin^2 \phi_0}, \quad \hat{y} &= \hat{x} + \tan \phi_0 \\ \hat{x}(0 +) &= 0, \hat{x}'(0 +) = I_0 / L = A \end{split}$$

where the normalized stiffness and damping forces are defined as $f_s = F_s/(Lk_g)$ and $f_d = F_d/(L\omega_n d_g)$, respectively, with $\hat{x} = x/L$, $\beta = k_i/k_g$, $\mu = d_g/d_i$, $t^* = \omega_n t$ and $\omega_n = \sqrt{(k_g + 2k_i \sin^2\phi_0)/M}$. Moreover, prime in (3) denotes differentiation with respect to the non-dimensional time, t^* , and the frequency ω_n denotes the linearized natural frequency of the oscillator, i.e., the approximate frequency of oscillation (in the absence of damping) in the limit of low-intensity impulses (or, equivalently, energies). The normalized system (3) will be the basis of the numerical simulations and theoretical analysis of Sections 3 and 4.

In Figs. 2a and 4 we depict the nonlinear stiffness and damping forces as functions of the normalized displacement \hat{x} and velocity \hat{x}' , for several initial angles of inclination, ϕ_0 , and the specific system parameters listed in Table 1. These correspond to the non-dimensional parameters $\beta=83.333$, and depending on the configuration of the system, to $\mu=0$ and/or $\beta=0$ (for the purely nonlinear damping and/or purely linear stiffness case — $d_g=0$ and/or $k_i=0$, respectively), or $\mu\to\infty$ and/or $\beta\to\infty$ (for the purely linear damping and/or purely nonlinear stiffness case — $d_i=0$ and/or $k_g=0$, respectively). Additionally, to better illustrate the positive or negative nonlinear stiffness characteristics generated due to geometric effects, we provide the plots of Fig. 2b which depict the derivative of the force produced by the springs with respect to the normalized displacement. The analytical expression for the derivative of the spring force with respect to the displacement is expressed as:

$$\frac{\partial f_s}{\partial \hat{y}} = \frac{1}{1 + 2\beta \sin^2 \phi_0} \left[1 + 2\beta - 2\beta \sec \phi_0 \frac{\sqrt{1 + \hat{y}^2} - \hat{y}^2 (1 + \hat{y}^2)^{-1/2}}{1 + \hat{y}^2} \right]$$
(4)

Moreover, unless otherwise indicated, all the numerical results presented herein are obtained using this specific set of system parameters.

The plots shown in Fig. 2 highlight the strong stiffness nonlinearity induced by the inclined springs for several initial angles, ϕ_0 . Considering the case $\phi_0=0$, we note that the derivative $df_s/d\hat{x}$ is always positive, and its value increases as the value of normalized displacement increases; this implies that the oscillator has *hardening* stiffness nonlinearity. However, for $\phi_0=9.37^\circ$ and $\phi_0=18.73^\circ$ there are ranges of the normalized displacement where $df_s/d\hat{x}<0$, whereas in complementary ranges of the normalized displacement $df_s/d\hat{x}>0$; it follows that, contrary to the previous case, the stiffness nonlinearity can be either *softening or hardening* as the system experiences positive to negative (or negative to positive) stiffness transitions depending on the

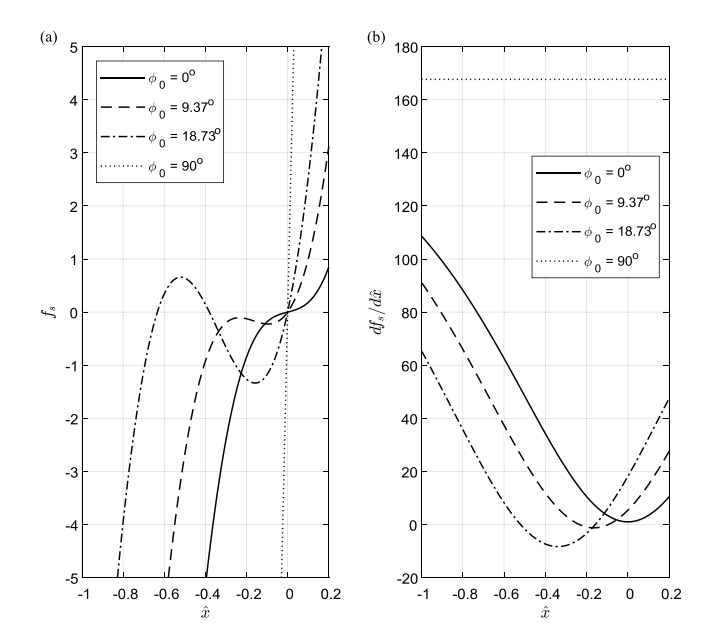


Fig. 2. Normalized nonlinear spring (a) force and (b) derivative provided by the inclined element with respect to the normalized displacement for different angles of inclination.

amplitude of the oscillation. Finally, in the limiting case $\phi_0=90^\circ$ the inclined spring–damper terms become vertical, and the stiffness of the oscillator is linear. These observations will be discussed later in more detail.

These results are caused by two bifurcations which can be analytically studied when the normalized stiffness force is considered as a function of the initial angle of inclination, ϕ_0 . The first bifurcation occurs at $\phi_0=\phi_{0,b1}\equiv\cos^{-1}[2\beta/(2\beta+1)]$ where $df_s/d\hat{x}=0$ at $\hat{x}=-\tan\phi_0$; that is, for initial angles of inclination greater than $\phi_{0,b1}$ the derivative $df_s/d\hat{x}$ vanishes at specific values of the normalized displacement, yielding zero effective stiffness at these points. Hence, for $\phi_0<\phi_{0,b1}$ the oscillator has positive stiffness, whereas for $\phi_0>\phi_{0,b1}$ there exist ranges of the oscillation amplitude where the overall effective stiffness is negative, so that the oscillator possesses stronger softening stiffness nonlinearity. The second bifurcation occurs at the angle of initial inclination where, along with the single equilibrium position, two new stable and unstable equilibria are generated. This bifurcation point is computed as

$$\phi_0 = \phi_{0,b2} \equiv \cos^{-1} \left[\frac{2\beta - 1}{(4\beta + 4)\sqrt{\beta(\beta + 1)/(4\beta^2 - 1)}} \right] > \phi_{0,b1}$$
 (5)

For $\phi_0 > \phi_{0,b2}$ there are two stable attractors for the transient dynamics of the oscillator (together with an unstable point); depending on the specific initial conditions of the system the dynamics may be attracted to either of the stable equilibria. It can be analytically and numerically shown that the following necessary and sufficient conditions for saddle-point bifurcation hold,

$$\begin{split} & f_s(\hat{y},\phi_0)\big|_{\substack{\hat{y}=\hat{y}_e\\ \phi_0=\phi_{0,b2}}} = \partial f_s(\hat{y},\phi_0)/\partial \hat{y}\big|_{\substack{\hat{y}=\hat{y}_e\\ \phi_0=\phi_{0,b2}}} = 0, \\ & \left[\left. \partial^2 f_s(\hat{y},\phi_0)/\partial \hat{y}^2 \right|_{\substack{\hat{y}=\hat{y}_e\\ \phi_0=\phi_{0,b2}}} \right] < 0, \left[\left. \partial f_s(\hat{y},\phi_0)/\partial \phi_0 \right|_{\substack{\hat{y}=\hat{y}_e\\ \phi_0=\phi_{0,b2}}} \right] > 0, \end{split}$$

where \hat{y}_e is the newly generated equilibrium point at the bifurcation point (cf. Fig. 3). These conditions indicate that this is indeed a saddle-node bifurcation point. Fig. 3 depicts the locus of the equilibrium positions of the system for various initial angles of inclination, ϕ_0 , and $\beta=200$.

According to the bifurcation plot of Fig. 3, before the bifurcation point, there exists only one stable equilibrium position, whereas after

(3)

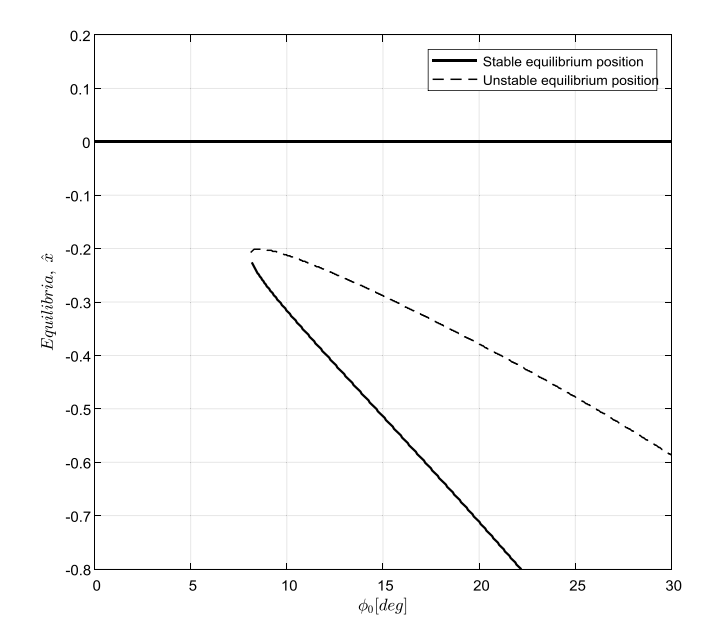


Fig. 3. Stable (solid curves) and unstable (dashed curves) equilibrium positions of the system as a function of initial inclination angle, ϕ_0 , for $\beta = 200$.

the bifurcation point, $\phi_0 > \phi_{0,b2}$, two additional equilibrium positions appear alongside the previous stable equilibrium. Applying linear perturbation analysis about each equilibrium one can easily determine the stability of each equilibrium positions as shown in Fig. 3.

In Fig. 4(a, b) we depict the corresponding nonlinear damping force as a function of normalized displacement and velocity while assuming that $\mu = 0$, i.e., the case of no grounding linear viscous damper — $d_{\sigma} = 0$. In these plots we include the overall linear damping force

corresponding to $\phi_0=90^\circ$ in order to highlight the difference between the linear and geometrically nonlinear cases. These curves show the strong geometric effects on the overall nonlinear damping force, and especially the striking differences in the nonlinear damping forces for different initial angles of inclination. The effect of the geometrically induced nonlinear dissipative terms on the dynamics of the impulsively forced oscillator will be discussed in detail in the next sections.

3. Transient nonlinear dynamics

In this section we study the nonlinear transient (decaying) impulsive response of the oscillator of Fig. 1. Our principal aim is to study the influence of the combined effects of geometrically nonlinear damping and stiffness in the transient dynamics and, in particular, to investigate how the hardening–softening nonlinear stiffness characteristics affect the transient response. To this end, we performed a series of numerical simulations by numerically integrating the strongly nonlinear equation of motion (1) subject to the specified initial conditions that correspond to impulsive excitation at the time instant $t^*=0$.

In Fig. 5(a, c) we depict the response of the system obtained by numerically integrating the equation of motion (1), together with its wavelet transform spectrum for the case corresponding to $\mu=0$, i.e., when the only dissipative forces are those produced by the geometrically nonlinear dampers, subjected to an applied initial impulse, $I_0=20$, and angle of inclination, $\phi_0=0$. For comparison, in Fig. 5(b, d) we consider the corresponding results when only linear dissipative forces exist in the system, under identical impulse excitation and angle of initial inclination. A first conclusion is that the purely nonlinear damping changes drastically the time decay of the transient response, in the sense that it slows considerably the dynamics. This indicates the presence of a much slower time scale in the transient dynamics compared to the case of purely linear viscous damping.

Furthermore, to physically interpret the transient responses in Fig. 5 we refer to the nonlinear stiffness plots depicted in Fig. 2. For the

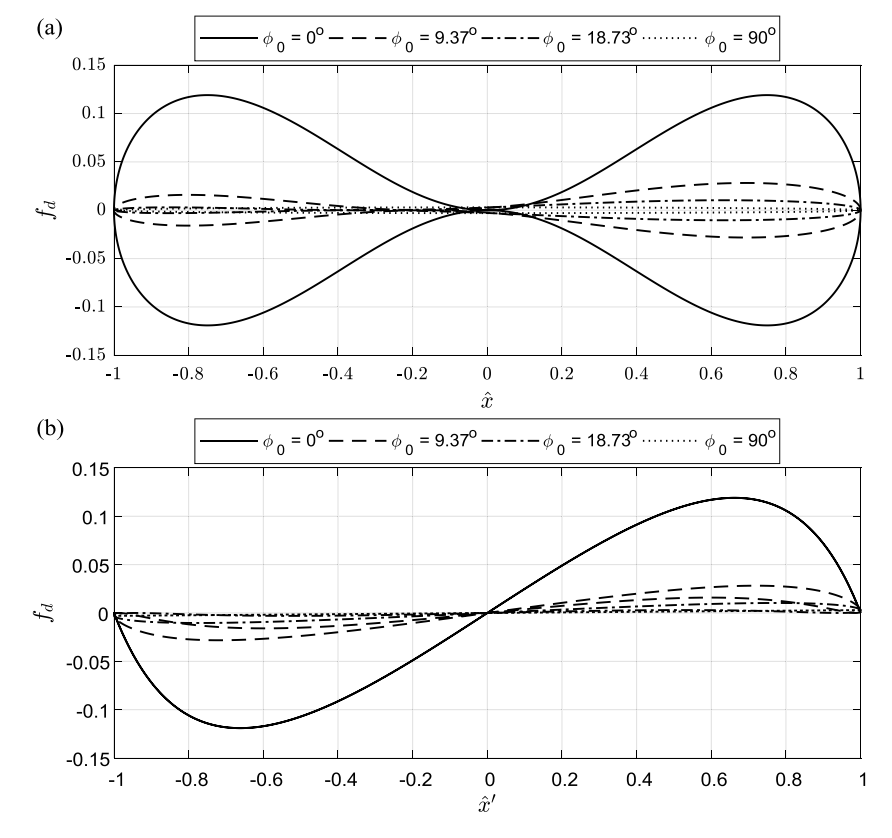


Fig. 4. Normalized damping force as function of (a) the normalized displacement and (b) the normalized velocity.

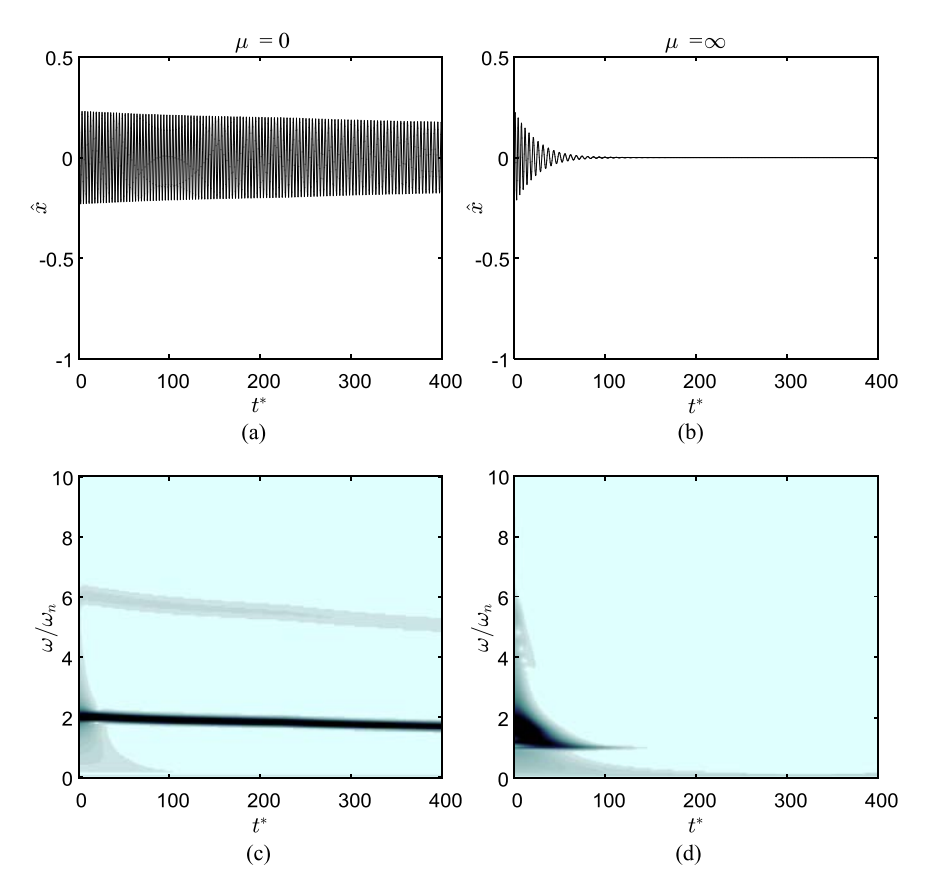


Fig. 5. Normalized time response of the system subject to the normalized initial impulse $I_0 = 20$, for the initial angle of inclination $\phi_0 = 0$: (a) Purely geometrically nonlinear damping $(\mu = 0)$, and (b) purely linear viscous damping $(\mu \to \infty)$; the corresponding wavelet spectra of these responses are depicted in (c) and (d).

case of geometrically nonlinear damping and stiffness – cf. Fig. 5(a,c) – the nonlinear force is both odd and symmetric. The symmetry of the nonlinear stiffness force should yield symmetric oscillations about the zero equilibrium of the mass about the zero equilibrium, and this is confirmed by the plot of Fig. 5(a). Moreover, the fact that the nonlinear stiffness is an odd function of the displacement should yield only odd harmonics in the wavelet spectrum of Fig. 5(c), which is again confirmed by the fact that a strong third harmonic (and higher odd harmonics) exists in that plot. Equivalently, since the force produced by the springs is an odd function of the displacement, the Taylor series expansion of the force only admits odd powers of the displacement (cf. Appendix). By replacing this force by its Taylor series expansion in (3) and performing harmonic balance one notes that only terms with frequencies equal to odd factors of the fundamental harmonic contribute to the free response of the system. We note that the presence of higher harmonics in the response strongly depends on the input energy to the system. The same observations hold for the case of linear viscous damping and geometrically nonlinear stiffness - cf. Fig. 5(b, d); however, in this case the decay of the transient response occurs on a strikingly faster time scale. Lastly, the hardening behavior of the stiffness nonlinearity is clear, since the decrease of the energy of the system (due to nonlinear or linear dissipation) leads to the decrease of the frequencies of the main harmonics of the response. In particular, the frequencies of the dominant (fundamental) harmonics in the wavelet spectra of Fig. 5(c) and (d) monotonically decrease with increasing time (or, equivalently, with decreasing energy) reaching eventually the asymptotic limit $\omega/\omega_n = 1$, where $\omega_n = \sqrt{k_g/M}$ is the linearized natural frequency of the oscillator in the low energy regime; we note, however, the strikingly slow rate of convergence of the dominant harmonic to this asymptotic limit in the case of nonlinear damping in Fig. 5(c).

In Fig. 6(a-d) we depict the responses and corresponding wavelet spectra of the oscillator with non-zero initial angle of inclination,

 $\phi_0 = 9.37^{\circ}$. We note that this angle is above the critical threshold corresponding to the first bifurcation but less than that corresponding to the second bifurcation. It follows that, in this case and in contrast to the case of $\phi_0 = 0$, the geometrically nonlinear springs force is neither symmetric nor odd with respect to the displacement (cf. Fig. 2). Lacking these features the impulsive response of the oscillator is not symmetric about the zero equilibrium; that is, the mean of the response time-series is non-zero and varies as the energy of the oscillator decreases. An additional consequence is the existence of even as well as odd harmonics in the wavelet spectra of Fig. 6(c) and (d). However, perhaps the main qualitative difference between this case and the previous one is that now the oscillator exhibits both hardening as well as softening nonlinear behavior in the initial and latter parts of the response, respectively. Indeed, up to $t^* \approx 500$ the oscillations exhibit hardening behavior as the normalized frequencies of the main and the higher harmonics decrease with decreasing energy; for larger times, however, these frequencies start to increase, with the dominant (fundamental) harmonic approaching the limiting linearized frequency, $\omega_n = \sqrt{(k_\sigma + 2k_i \sin^2 \phi_0)/M}$. Similar to the previous case of zero angle of initial inclination, however, we deduce that for the case of nonlinear damping the decaying transient response is governed by a much slower time scale compared to the case of linear viscous damping.

Finally, in Fig. 7 we depict the impulsive response of the oscillator for the initial angle of inclination, $\phi_0 = 18.73^\circ$. Again, the oscillator exhibits strong hardening behavior until $t^* \approx 360$, after which the behavior abruptly switches to softening. In addition, as energy decreases sufficiently the dynamics approach the linear limit, and the frequency of the dominant harmonic approaches the normalized linearized frequency $\omega_n = \sqrt{(k_g + 2k_i \sin^2 \phi_0)/M}$. In this case the initial angle of inclination exceeds the critical threshold for the second bifurcation, so the response of the oscillator exhibits bi-stability in the initial, highly energetic

regime of the response. This yields significantly stronger and more broadband energy scattering to higher frequencies compared to the previous two cases, a feature that is clearly visible in the corresponding wavelet spectra. Moreover, the switch between the (early) hardening and the (later) softening behavior is much more abrupt compared to the case with $\phi_0=9.37^\circ$, which again is attributed to the initial bi-stable response regime which is absent in the prior case.

In the next section we analytically study the damped transient dynamics by a methodology that combines slow-fast partitions and complexification-averaging (CX-A). The time series depicted in Figs. 5–7 are amenable to such an analysis as they are composed of "fast" oscillations (i.e., the fast parts of the dynamics) that are modulated by "slow" envelopes (or slow modulations — the slow parts of the dynamics). By studying the time evolutions of the envelopes (i.e., the slow dynamics) we will be able to identify the "slowing down" of the transient dynamics induced by the geometrically nonlinear damping observed in the previous numerical simulations.

4. slow-fast partition of the dynamics and slow flow analysis

The analysis in this section will consider the normalized oscillator (3). To apply the complexification-averaging (CX-A) method of analysis it is convenient to replace the geometrically exact expressions for the nonlinear spring and damping forces – Eq. (3) – by truncated, approximate expressions derived by Taylor-series expansions of the exact formulas. The resulting polynomial expressions will be amenable for CX-A analysis.

4.1. Taylor series approximation of the force exerted by the inclined element

To this end, the normalized expressions for the nonlinear forces are expanded in Taylor series up to the 6th order,

$$\begin{split} f_s &\approx \hat{f_s} = \frac{\left[1 + 2\beta \left(C_0 + C_1 \hat{x} + C_2 \hat{x}^2 + C_3 \hat{x}^3 + C_4 \hat{x}^4 + C_5 \hat{x}^5\right)\right] \hat{x}}{1 + 2\beta C_0} \\ f_d &\approx \hat{f_d} = \frac{\delta \left[\mu + 2\left(D_0 + D_1 \hat{x} + D_2 \hat{x}^2 + D_3 \hat{x}^3 + D_4 \hat{x}^4 + D_5 \hat{x}^5\right)\right] \hat{x}'}{1 + 2\beta C_0} \end{split} \tag{6}$$

where \hat{f}_s and \hat{f}_d denote the approximate truncated nonlinear spring and damping forces, $\delta = d_i \omega_n / k_g$, and the coefficients C_0 through C_5 , and D_0 through D_5 are listed in the Appendix. Based on these approximations the exact system (3) is replaced by the following approximate system,

$$\hat{x}'' + \hat{f}_s + \hat{f}_d = 0,$$

$$\hat{x}(0+) = 0, \hat{x}'(0+) = A$$
(7)

which will be the basis for the asymptotic analysis that follows.

However, before the CX-A analysis can commence it is necessary the assess the validity of the approximate system (6) and (7). Accordingly, a detailed numerical convergence study was undertaken to ensure that the approximate normalized restoring force $\hat{f}_s(t^*) + \hat{f}_d(t^*)$ based on the previous truncated Taylor-series expressions accurately reproduced the exact normalized restoring force $f_s(t^*) + f_d(t^*)$ in Eq. (3).

Some representative results of this convergence study are depicted in Figs. 8 and 9 that depict the restoring force time series for oscillators with initial angle of inclination 9.37° and 18.73°, respectively. We note that the Taylor-series approximations accurately reproduce the exact expressions. Moreover, the approximations accurately capture both the initial hardening and the later softening response regimes, as well as the abrupt end of the bi-stable oscillation regime for the larger initial angle of inclination (cf. Fig. 9 — which also signifies an abrupt qualitative change in the transient dynamics). Based on this convergence study we conclude that we may replace the exact system (3) with the simplified polynomial model (6–7) without compromising the validity of the asymptotic analysis.

4.2. Applying the complexification-averaging method (CX-A)

Proceeding now to the CX-A analysis, we define the new complex variable $\psi(t^*) = \hat{x}'(t^*) + i\,\hat{x}(t^*)$ where $i = \sqrt{-1}$, and express the normalized displacement and its derivatives as follow, $\hat{x} = -(i/2)(\psi - \overline{\psi})$, $\hat{x}' = (1/2)(\psi + \overline{\psi})$, and $\hat{x}'' = \frac{d\psi}{dt} - (i/2)(\psi + \overline{\psi})$, where overbar denotes complex conjugate and the dependence on the normalized time was omitted. Substituting these expressions into the approximate model (6–7) we complexify the dynamics and derive the following first-order complex differential equation:

$$\begin{split} \frac{d\psi}{dt} - (i/2)(\psi + \overline{\psi}) + \hat{f}_s \left[\hat{x} = -(i/2)(\psi - \overline{\psi}) \right] \\ + \hat{f}_d \left[\hat{x} = -(i/2)(\psi - \overline{\psi}), \ \hat{x}' = (1/2)(\psi + \overline{\psi}) \right] = 0, \end{split} \tag{8}$$

$$\psi(0+) = I_0$$

Whereas this operation might seem to complicate the analysis, its major advantage over system (7) is that it allows for a fast–slow partition of the transient dynamics. Indeed, motivated by the observation that the damped responses are in the form of "fast" oscillations that are modulated by "slow" envelopes (or modulations) we introduce a slowfast partition of the complex response as, $\psi(t^*) \approx \varphi(t^*)e^{it^*}$ where e^{it^*} represents the fast oscillation (with fast normalized frequency equal to unity), and $\varphi(t^*)$ its (complex) slow modulation. In that way we separate the slow and fast components of the system response. We note at this point that this particular slow-fast representation is only valid for the regime of the damped response where the fast oscillation contains a single dominant normalized fast frequency close to unity (or equivalently close to the linearized natural frequency ω_n in terms of physical time t). This implies that our analysis is valid in the later regime of the dynamics where the decaying normalized response is dominated by that fast frequency or relatively small initial angles of inclination where the frequency of the fundamental harmonic does not change significantly with respect to total energy of the system. In early regimes of the damped response, where the dominant fast frequencies are different than unity or there exist multiple dominant fast frequencies, the analysis is not valid, and the response cannot be captured by the present analysis. Nevertheless, our analysis will reveal the (slow) time scale of the decay of the damped oscillations and will prove that the geometrically nonlinear damping "slows down" the decay of the oscillations compared to linear viscous damping.

Substituting the previous slow–fast partition in (8), we express the complex equation of motion in terms of $\varphi(t^*)$. Then, the final step of the analysis is to average the resulting complex equation with respect to the fast frequency, which is equivalent to omitting fast components in the modulation equation with fast frequencies higher than unity. This yields the complex first-order differential equation governing the slow evolution of the envelope (or modulation) $\varphi(t^*)$,

$$\begin{split} 2\varphi' + i\varphi + \left(\delta \frac{\mu + 2D_0}{1 + 2\beta C_0} - i\right)\varphi + \frac{1}{2}\left(\frac{\delta D_2}{1 + 2\beta C_0} - \frac{3i\beta C_2}{1 + 2\beta C_0}\right)|\varphi|^2\varphi + \\ \frac{1}{8}\left(\frac{\delta D_4}{1 + 2\beta C_0} - \frac{5i\beta C_4}{1 + 2\beta C_0}\right)|\varphi|^4\varphi = 0, \\ \varphi(0+) &= I_0 \end{split} \tag{9}$$

where $\delta=d_i\omega_n/k_g$. Eq. (9) is referred to as the *slow-flow* which governs the slow-dynamics of the system after the (rather trivial) fast dynamics have been eliminated by the previous averaging operation. Introducing at this point the notation, $u=|\varphi|$, $\lambda_1=\delta\left(\mu+2D_0\right)/\left(1+2\beta C_0\right)$, $\lambda_2=\delta D_2/\left(2+4\beta C_0\right)$ and $\lambda_3=\delta D_4/\left(8+16\beta C_0\right)$, and performing straightforward algebraic manipulations, complex Eq. (9) reduces to the real first-order differential equation for the modulus of the slow modulation $\varphi(t^*)$,

$$2u' + \lambda_1 u + \lambda_2 u^3 + \lambda_3 u^5 = 0, u(0+) = I_0$$
(10)

This is referred to as the *real slow flow* of the problem, in contrast to the complex slow flow (9).

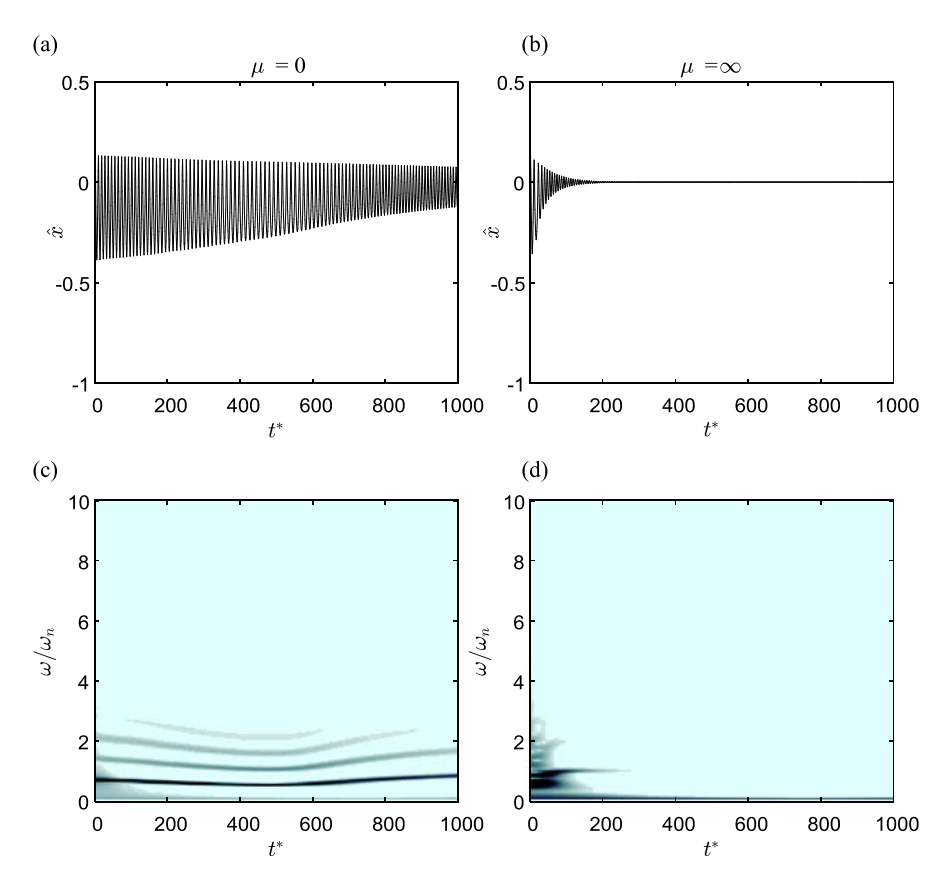


Fig. 6. Normalized time response of the system subject to the normalized initial impulse $I_0=20$, for the initial angle of inclination $\phi_0=9.37^\circ$: (a) Purely geometrically nonlinear damping ($\mu=0$), and (c) purely linear viscous damping ($\mu\to\infty$); the corresponding wavelet spectra of these responses are depicted in (b) and (d).

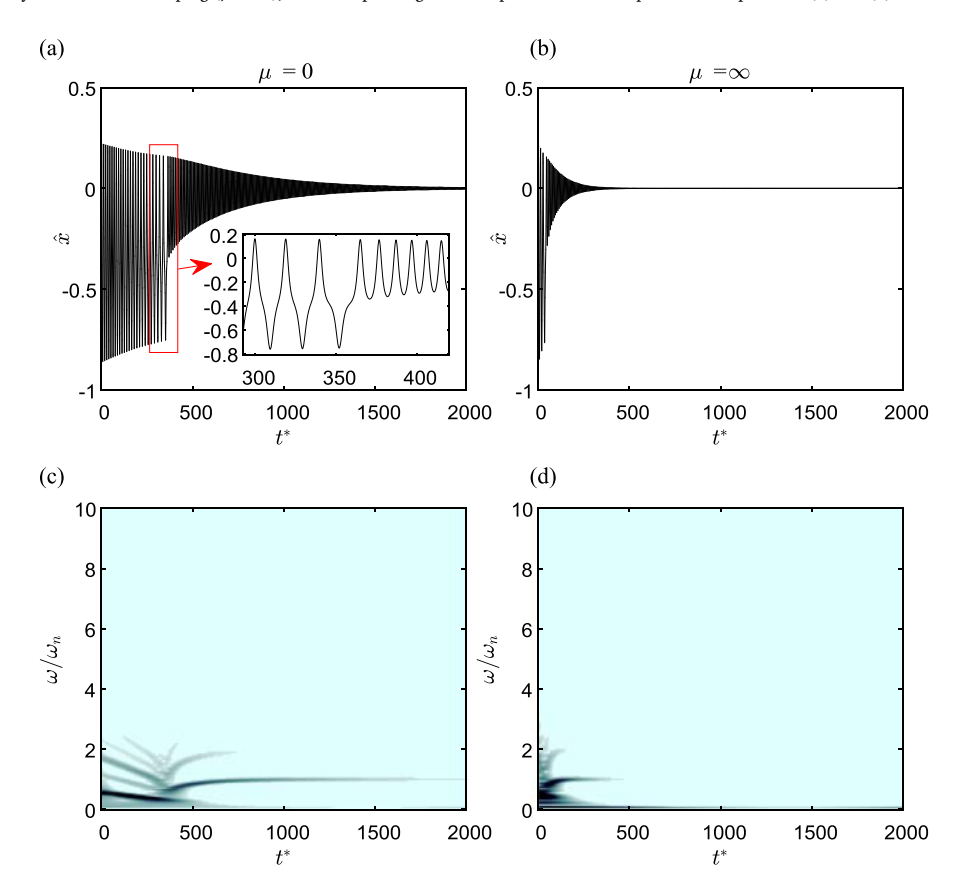


Fig. 7. Normalized time response of the system subject to the normalized initial impulse $I_0 = 60$, for the initial angle of inclination $\phi_0 = 18.73^\circ$: (a) Purely geometrically nonlinear damping ($\mu = 0$), and (c) purely linear viscous damping ($\mu \to \infty$); the corresponding wavelet spectra of these responses are depicted in (b) and (d).

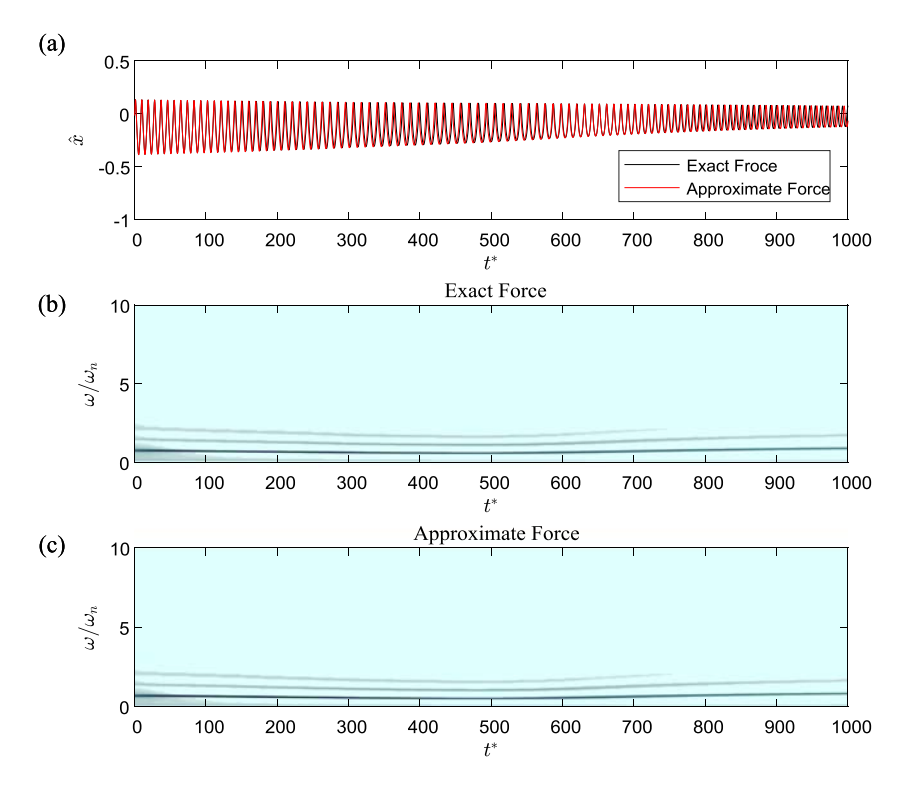


Fig. 8. Comparison of the exact restoring force obtained by superposition of the normalized nonlinear spring and damping forces in (3) with the corresponding approximate restoring force obtained by superposition of the forces in (6) derived by Taylor-series expansions: (a) Force time series for normalized initial impulse $I_0 = 20$ and initial angle of inclination $\phi_0 = 9.37^\circ$; corresponding wavelet spectrum of (b) the exact restoring force, and (c) the approximate restoring force.

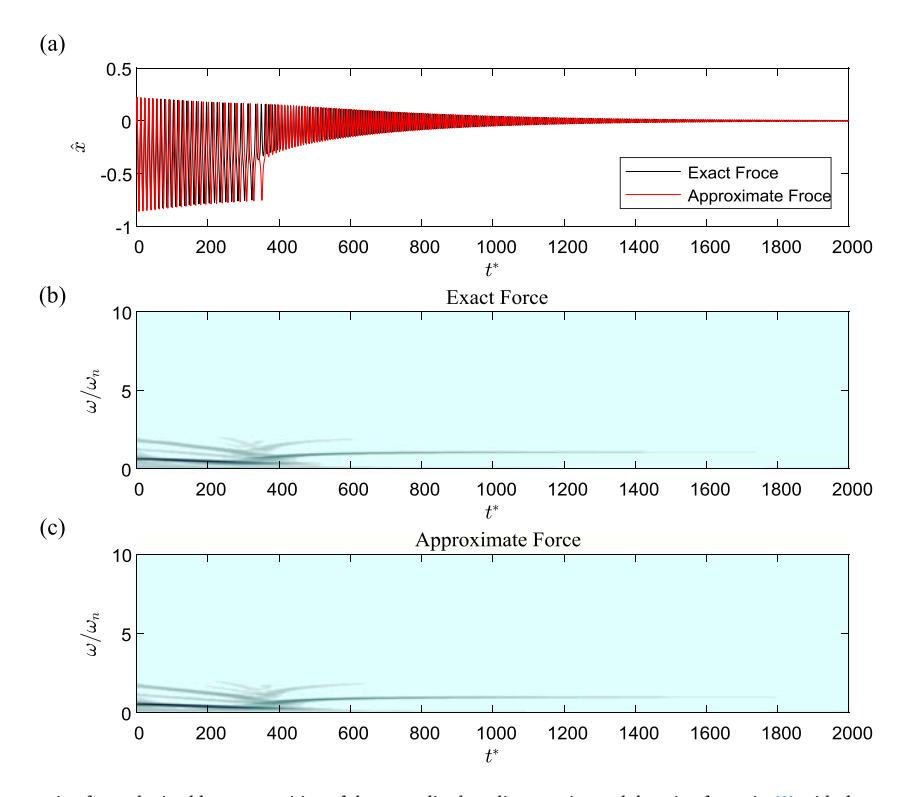


Fig. 9. Comparison of the exact restoring force obtained by superposition of the normalized nonlinear spring and damping forces in (3) with the corresponding approximate restoring force obtained by superposition of the forces in (6) derived by Taylor-series expansions: (a) Force time series for normalized initial impulse $I_0 = 60$ and initial angle of inclination $\phi_0 = 18.73^\circ$; corresponding wavelet spectrum of (b) the exact restoring force, and (c) the approximate restoring force.

Two representative examples confirming the validity of the analysis are now given. In Fig. 10(a) and (b) we show the comparison between the results from direct numerical integration of the exact oscillator (3) and the real slow flow (10) for two cases. Fig. 10(a) depicts the

response of the oscillator for the case of purely geometrically nonlinear damping ($\mu=0$) and nonlinear stiffness corresponding to an initial angle of inclination $\phi_0=9.37^\circ$, whereas Fig. 10(b) depicts the response of the oscillator for the same initial angle of inclination but with only

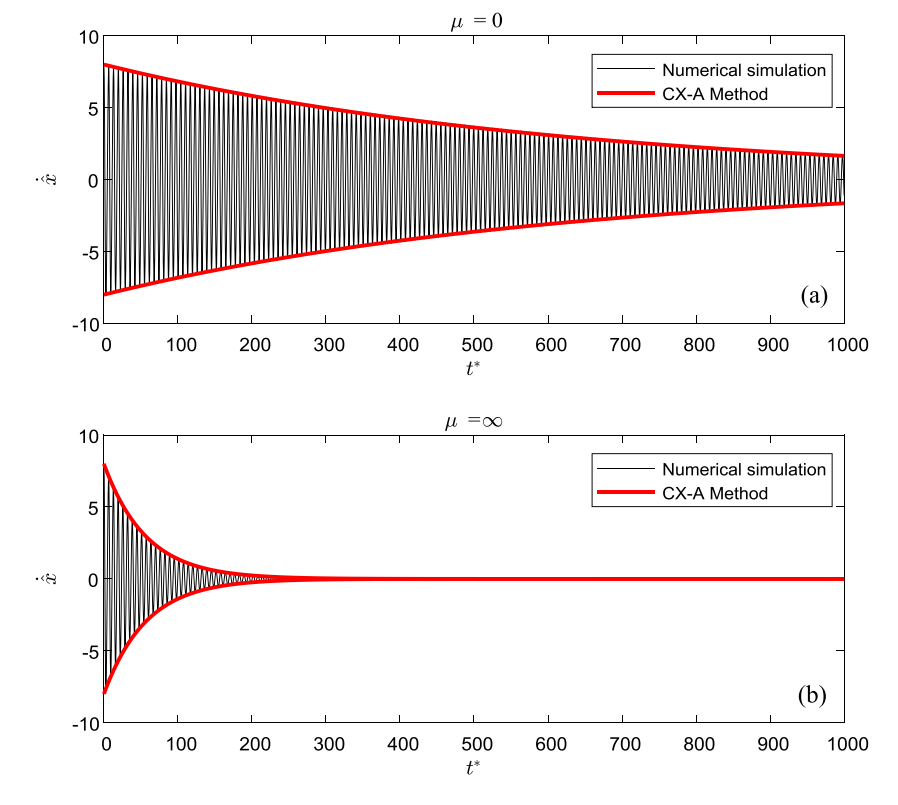


Fig. 10. Comparison between direct numerical integration of the exact oscillator (3) and the analytical prediction (10) for the oscillator with initial angle of inclination, $\phi_0 = 9.37^\circ$, and normalized impulse intensity $I_0 = 8$: (a) Purely nonlinear damping, $\mu = 0$, and (b) purely linear damping, $\mu \to \infty$.

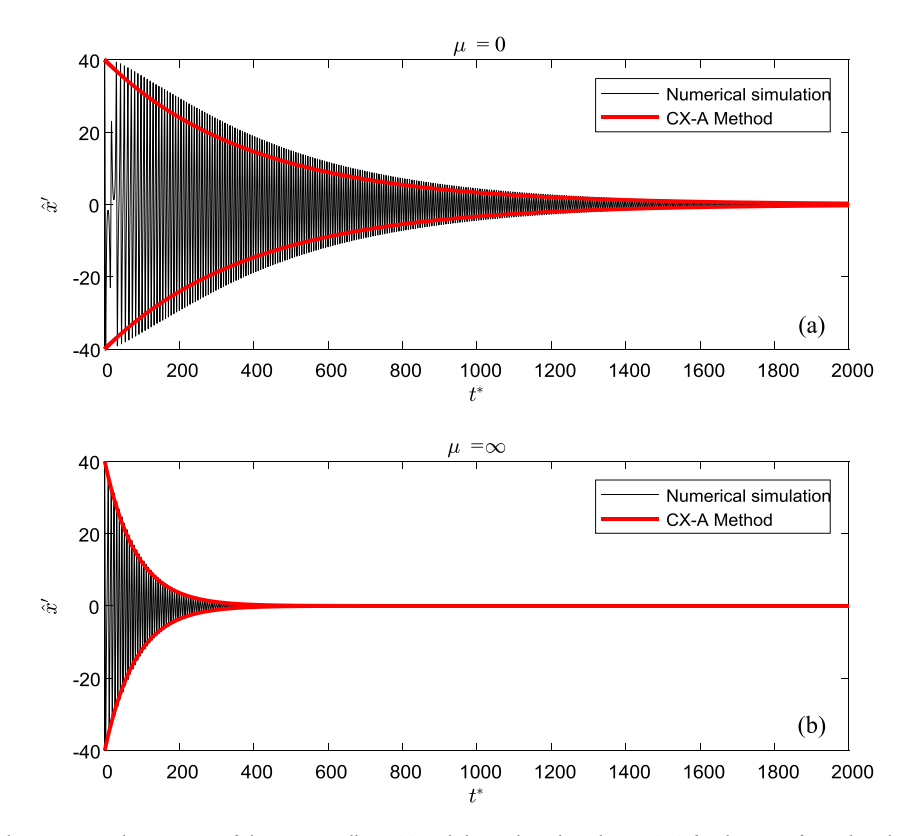


Fig. 11. Comparison between direct numerical integration of the exact oscillator (3) and the analytical prediction (10) for the case of initial angle of inclination, $\phi_0 = 18.73^\circ$, and normalized impulse intensity $I_0 = 40$: (a) Purely nonlinear damping, $\mu = 0$, and (b) purely linear damping, $\mu \to \infty$.

linear damping ($\mu \to \infty$). It is clear from these results that in this particular case the slow-flow Eq. (10) is capable of accurately capturing the rate of decay of the impulsive response for the entire duration of

the oscillation and not only in the later regime of the oscillation. This occurs since, for this relatively small angle ϕ_0 , the fast frequency is close to the normalized linearized frequency (i.e., unity), and as a result the

slow–fast partition and the CX-A methodology are valid for the entire oscillation. In the next example this is not so. In Fig. 11(a) and (b) we depict similar comparisons for the case of the larger angle $\phi_0=18.73^\circ$, where there is a bi-stable regime at the initial, highly energetic phase of the oscillation. During this initial (hardening) regime the oscillator undergoes transitions between the two stable bi-stable equilibrium points, and the oscillation is not governed by a fast frequency close to unity; as a result, the CX-A analysis is not valid there. However, with decreasing energy the oscillation switches to the softening regime which indeed is governed by a fast frequency close to unity, so the analytical prediction from (10) matches the decay of the amplitude in this lower-energy regime of the response.

Having established the validity of the CX-A analysis and its capacity to accurately predict the decay of the oscillation, we reconsider (10) and derive an approximate analytical solution for the envelope $u(t^*)$. To do this we take into account the fact that the CX-A method is valid in the later small-energy regime of the oscillation or, equivalently, under the assumption of small displacement. In that regime of the decaying response the highest power of u may be omitted in (10), and the resulting simplified first-order nonlinear ordinary differential equation can be solved by the separation of variables method and integration by quadratures. The resulting analytical solution is,

$$u(t^*) \simeq I_0 \sqrt{\frac{\lambda_1}{\lambda_1 \exp\left(\lambda_1 t^*\right) + \lambda_2 I_0^2 \left[\exp\left(\lambda_1 t^*\right) - 1\right]}}$$
 (11)

Following this, we define the decay time constant, τ , corresponding to the normalized time satisfying the condition $u(\tau)/u(0+)=0.01$. This yields the analytical expression for the time constant,

$$\tau = \frac{1}{\gamma} = \frac{1}{\lambda_1} \ln \left(\frac{10^4 \lambda_1 + \lambda_2 u_0^2}{\lambda_1 + \lambda_2 u_0^2} \right)$$
 (12)

where γ is the decay rate of the damped response. We note at this point that the analytical approximations (11) and (12) are based on the truncated (up to the sixth-order) approximate oscillator (6–7), so they are valid only for relatively small values of the initial angle of inclination, ϕ_0 . Nevertheless, these analytical estimates prove and predict the increase of the decay time constant of the oscillator due to geometrically nonlinear damping.

To this end, we introduce the linear and nonlinear decay time constants $\tau_{NL}(\phi_0)$ and $\tau_{Lin.}$, corresponding to oscillators with purely linear and purely nonlinear damping,

$$\tau_{NL}(\phi_0) = \frac{1}{\gamma_{NL}(\phi_0)} \approx \frac{4M}{2d_i \sin^2 \phi_0} \ln(10)$$

$$\tau_{Lin} = \frac{1}{\gamma_{Lin}} \approx \frac{4M}{d_\sigma} \ln(10)$$
(13)

and show that

$$\frac{\tau_{NL}(\phi_0)}{\tau_{Lin}} = \frac{\gamma_{Lin}}{\gamma_{NL}(\phi_0)} = \frac{d_g}{2d_i \sin^2 \phi_0}$$
 (14)

Moreover, for the specific choice of damping parameters, $d_g = 2d_i$ (which indeed corresponds to the selected system parameters listed in Table 1), this relation simplifies to,

$$\frac{\tau_{NL}(\phi_0)}{\tau_{Lin}} = \frac{1}{\sin^2 \phi_0} \simeq \frac{1}{\phi_0^2}, \quad d_g = 2d_i, \quad \sin \phi_0 \ll 1$$
 (15)

for sufficiently small initial angles of inclination. The analytical results (14) and (15) provide the quantification of the increase of the decay time constant (or equivalently, the decrease of the decay rate) of the impulsive response of the nonlinear oscillator due to geometrically nonlinear damping.

In Fig. 12 we depict the comparison, between the results of CX-A analysis and direct numerical simulation of system (3), of the logarithmic decays of the normalized velocity \hat{x}' for normalized impulse intensity $I_0=8$ and different initial angles of inclination. Clear agreement between analysis and numerical simulation is noted, which further

Table 2 Ratios of the velocity logarithmic decays of Fig. 12 for the cases of geometrically nonlinear $(\mu = 0)$ and linear $(\mu \to \infty)$ damping, predicted by analysis and simulation.

	Slope ratio (CX-A)	Slope ratio (Simulation)	$ au_{Lin}/ au_{NL} \simeq \phi_0^2$
$\phi_0 = 0^{\circ}$	0.0012	0.0111	0
$\phi_0 = 9.37^{\circ}$	0.0212	0.0232	0.0267
$\phi_0 = 12.23^{\circ}$	0.0299	0.0311	0.0456

confirms the validity of the CX-A analysis and highlights the slower time scale governing the response decay due to geometric damping. An additional quantification of the results of Fig. 12 is provided in Table 2 which validates numerically the approximate theoretical prediction (15). The numerical results in that Table compute the ratios of the velocity logarithmic decays of Fig. 12 for geometrically nonlinear ($\mu=0$) and linear ($\mu\to\infty$) damping, predicted by the CX-A analysis or computed by direct numerical simulation of system (3). Again, the theoretical result accurately predicts the logarithmic decay and quantifies the slower rate of response decay due to geometrically nonlinear damping.

These results complete the theoretical study of the impulsive response of the nonlinear oscillator (3). In the next section an experimental study is performed to validate the theoretical predictions. The experimental fixture consists of a clamped-free linear beam with inclined parallel springs at its end; only the first bending mode of the beam is considered in the study in order to approximate the theoretical model of Fig. 1. For the experimental study we will revert to dimensional parameters.

5. Experimental study and theoretical validation

The experimental fixture is shown in Fig. 13. It consists of a uniform beam clamped at one of its ends and pinned at its other end to a pair of identical inclined parallel springs. The length of each spring is 76.2 mm, its inner diameter is 19.3 mm and the diameter of its wire is 2.67 mm. The neutral length of the moving part of the attachment supporting each spring is 0.15 m due to bolts that are attached to both ends of the spring — cf. Fig. 13(a, b). Due to its internal structural damping (which is identified below), each of the experimental springs acts, in essence, as a spring-damper pair in parallel. The beam is made of lowcarbon steel with density 7784 kg/m 3 , length 1.676 m, and cross-section 0.045×0.008 m². The modulus of elasticity of the beam is estimated to be 192 GPa by means of an optimization computation discussed below. A PCB Piezotronics shear accelerometer (model 353B15) with nominal sensitivity of 1.100 mV/ (m/s^2) is attached close to the tip of the beam (at a distance of 1.65 m from the clamped end of the beam) right at the location where the inclined attachment is pinned. The entire fixture is installed on an optical table which serves as ground.

Since the theoretical study of the previous sections was based on the assumption that the inclined spring-damper elements in the system of Fig. 1 are pinned to the mass, in the experimental setup each of the inclined springs was connected to the beam by bolting one of its ends to a steel shaft (roller) which passed through two Teflon sleeve bearings made of PTFE that are firmly attached to the tip of the beam; a detail of the pinned connection is provided in Fig. 13(c). Teflon sleeve bearings were selected to reduce friction in the pinned joints as much as possible. Similarly, the other end of each of the inclined springs is grounded by securing that end to a roller that is attached to a vertical threaded rod bolted to the optical table (which acted as "ground" for the experimental fixture). Note that the lengths and stiffnesses of the inclined springs were chosen so that they do not buckle under small compression loads. Moreover, to ensure the least amount of residual pre-tension or precompression of the inclined springs when varying their initial angle of inclination, while still attached to the beam we unbolt their grounded connection (the threaded vertical rod) and rotate the entire attachment until we find a threaded hole on the optical table so that in its new position the inclined pair of springs is nearly unstretched. This ensures

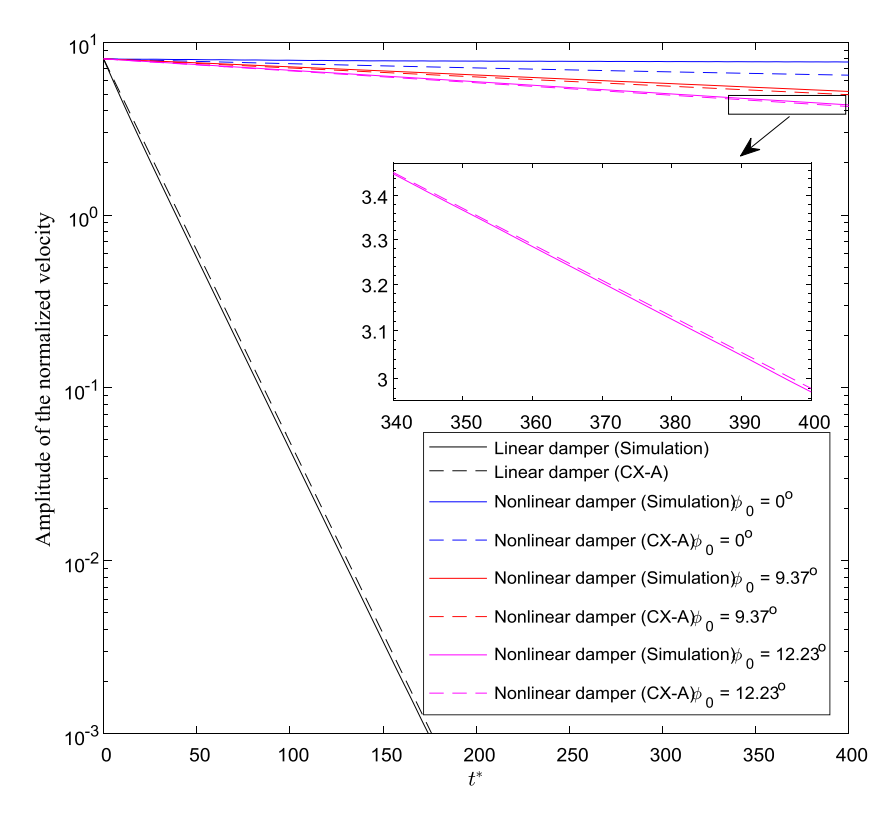


Fig. 12. Comparison between the predicted logarithmic decay rate of the normalized velocity obtained by the slow flow (9) and direct numerical integration of the exact oscillator (3) for $I_0 = 8$, and different angles of initial inclination.

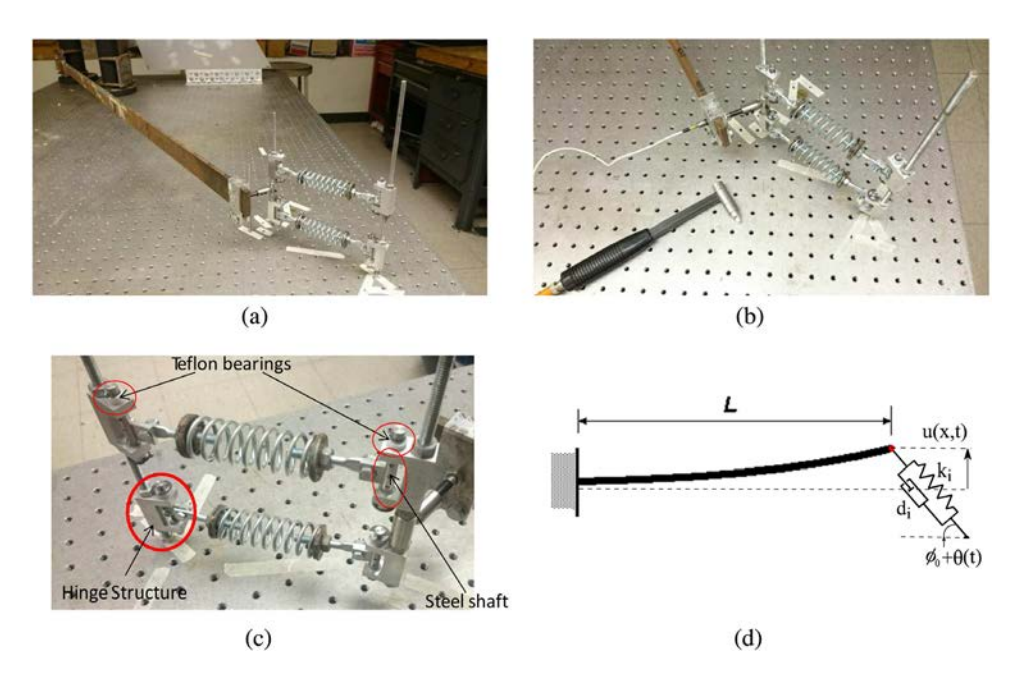


Fig. 13. Experimental fixture: (a) Beam with pinned pair of parallel inclined springs, (b, c) detail of the pinned connection, and (d) associated mathematical model.

that the attachment is close to its natural length when the system is at equilibrium and satisfies this basic assumption of the theoretical study. Finally, we note that an axial force is applied to the beam by the inclined attachment during the transient response. Since the axial stiffness of the beam is much larger compared to its transverse stiffness (we estimated that the natural frequencies for axial oscillations of the beam are much higher compared to those of the leading-order transverse modes. For instance, the natural frequency corresponding to the first axial mode of

vibration of the beam is computed to be 740.65 Hz which indicates that the axial stiffness of the beam is much greater than that of the leading-order transverse modes), the resulting axial deformation of the beam is orders of magnitude smaller than the transverse deformation, so it can be neglected. The associated mathematical model of the experimental fixture is shown in Fig. 13(d). A regime of small oscillations is assumed, so in the mathematical model the beam is based on first-order Euler–Bernoulli linear beam theory.

Table 3Results of the experimental modal analysis of the uncoupled beam.

Mode No. Nat. Freq. [Hz]		Modal damping ratio	
1	2.126	0.0253	
2	13.391	0.0019	
3	37.975	0.0010	

We note at this point that the beam has an infinite number of bending modes and as such differs from the simplified oscillator depicted in Fig. 1; nevertheless, by considering the response of only the first bending mode (i.e., by confining our attention to the frequency range close to the first bending mode) it should be possible to approximately reproduce the theoretical system in the experiment. Of course, this hypothesis neglects the effects of the higher bending modes to the beam response, but it is assumed that these higher frequency effects are much smaller in the range of energies and frequencies considered in the present experimental study.

5.1. Linear modal analysis and parameter identification

In the first phase of the experimental study we perform (linear) modal analysis of the clamped-free beam by disconnecting the inclined springs and referring to it as the "uncoupled beam." This task is performed to experimentally identify the natural frequency and modal damping of each of the leading bending modes of the uncoupled (linear) beam. To perform this study the beam is forced by an impulsive excitation using a modal impact hammer (PCB model 086C01) at the location where the accelerometer is attached — cf. Fig. 14(a). We note that in the experiments with the coupled (geometrically nonlinear) system i.e., the beam connected to the spring elements - that were performed for the purpose of validating the theoretical study, the beam was excited differently, namely by prescribing an initial tip displacement. Since the internal damping of the plain beam was observed to be very low, all the data used for the linear modal analysis was recorded at a 40.96 kHz sampling frequency for 52.2 s to capture the decay of the response more accurately using the Polytec Scanning Vibrometer software (version 8.722). In the later experiments with the integrated system, however, the data used for the theoretical validation was recorded at a 20.48 kHz sampling frequency for at least 12.8 s using the same software. After the acceleration time series of the tip of the plain beam was recorded by the accelerometer, the corresponding velocity and displacement time series were computed by numerically integrating the measured accelerations and the computed velocities, respectively. After each integration, a third-order high-pass Butterworth filter with cutoff frequency of 1 Hz was applied to remove the artificial low frequency component added to the signal due to numerical integration. In addition, the temporal non-zero constant or linearly increasing/decreasing mean-value of each time signal was removed before and after each integration. An impulse of maximum magnitude 491.2 N is applied by the modal hammer at the tip of the beam, and the measured response time series is post-processed for modal analysis. Assuming proportional modal damping, the modal parameters of the uncoupled beam are extracted by applying the RFP method [25], and the results of the experimental modal analysis are listed in Table 3 for the leading three modes of the beam.

Based on the identified modal parameters of the uncoupled beam, a computational finite element (FE) model is created using 16 Euler–Bernoulli beam elements. The Young's modulus of the FE model is obtained by applying natural frequency optimization to minimize the accumulate relative error between the natural frequencies of the first four bending modes of the beam and those measured from the experiment, whereas the proportional damping matrix is obtained by matching the experimental modal damping ratios. The optimized Young's modulus is computed as 192 GPa. In Fig. 14(a) we depict the applied experimental impulse, and in Fig. 14(b–e) the comparison between the experimental and computational responses of the uncoupled beam. From these results

 Table 4

 Identified parameters for the system of parallel springs in the inclined attachment.

Attachment	Unstretched length, l_0 [m]	0.0762
	Mass of springs, m_{springs} [kg]	0.1400
	Added mass at the tip, m_{tip} [kg]	0.1955
	Linear stiffness, k_{springs} [N/m]	6816.0517
	Linear viscous damping, d _{springs} [N s/m]	0.7492

it is clear that the computational model captures accurately at least the leading three bending modes of the uncoupled system; regarding higher modes it is anticipated that their contribution to the response is small and can be neglected.

In the second phase of the experimental study the linear stiffness and viscous damping properties of the pair of inclined springs is identified. To this end, the inclined element is placed in a perpendicular position to the beam (i.e., at an initial angle of inclination $\phi_0 = 90^{\circ}$), so there should be complete absence of geometric nonlinearities in the dynamics, and the impulsive response of the coupled beam-springs system should be linear. We refer to this system as the "coupled system." Taking into account the previously identified modal properties of the uncoupled beam, a second experimental modal analysis is performed for the coupled system, and the revised modal properties are again experimentally identified with the RFP method. Then, the previous computational FE model of the uncoupled beam is augmented with the perpendicular system of parallel springs, and the stiffness and damping properties of the springs are identified by natural frequency and modal damping optimization, i.e., by matching the experimental and computational natural frequencies and modal damping ratios of the integrated system for the first four bending modes of the beam. In Table 4 we list the resulting identified parameters for the two parallel springs, which completes the computational model.

In Fig. 15 we depict the results of the experimental modal analysis of the coupled beam subject to an applied impulsive load of similar magnitude and duration with that shown in Fig. 14(a). In Fig. 15(ad) we present the comparison between the experimental and computational responses of the coupled beam. Comparing these results with the corresponding plots of Fig. 14, we note the significant and rapid reduction of the transient oscillations due to the overall stiffening of the system and the added damping provided by the attachment. From these results it is also clear that the computational model again captures accurately the leading in-plane bending modes of the uncoupled system. The mode at 66 Hz we conjecture to be a torsional mode and the mode at 78 Hz is the natural frequency of an out of plane bending mode of the beam (cf. Fig. 14). It should be mentioned that the mismatch between the model and the experiment for the modes above the third in-plane bending modes is irrelevant for our study which is primarily based on the response of the first (fundamental) bending mode of the beam.

5.2. Experimental results—Beam with the inclined spring-damper attached to its free end

After modal analysis and construction of the FE of the coupled beam, the third and final experimental phase was performed, with the basic aim being the verification of the theoretical predictions. A series of experimental tests was performed by fixing the inclined element to a (small) initial angle, ϕ_0 , and applying an initial tip displacement to the beam which is expected to excite primarily the first bending mode. In Figs. 16–18 we depict some typical results, comparing the experimental and computational velocity time series. In Fig. 16 we consider an initial angle of inclination, $\phi_0 = 20^\circ$, and initial tip displacement, $u_0 = -0.060\,\mathrm{m}$. The results in Fig. 17 correspond to the initial angle of inclination, $\phi_0 = 16.5^\circ$, and same initial tip displacement, $u_0 = -0.060\,\mathrm{m}$. Finally, in Fig. 18 we consider the case $\phi_0 = 16.5^\circ$ and $u_0 = -0.050\,\mathrm{m}$. Each experimental or computational velocity time series was post-processed by wavelet-bounded Empirical Mode Decomposition (WBEMD) to obtain the corresponding dominant

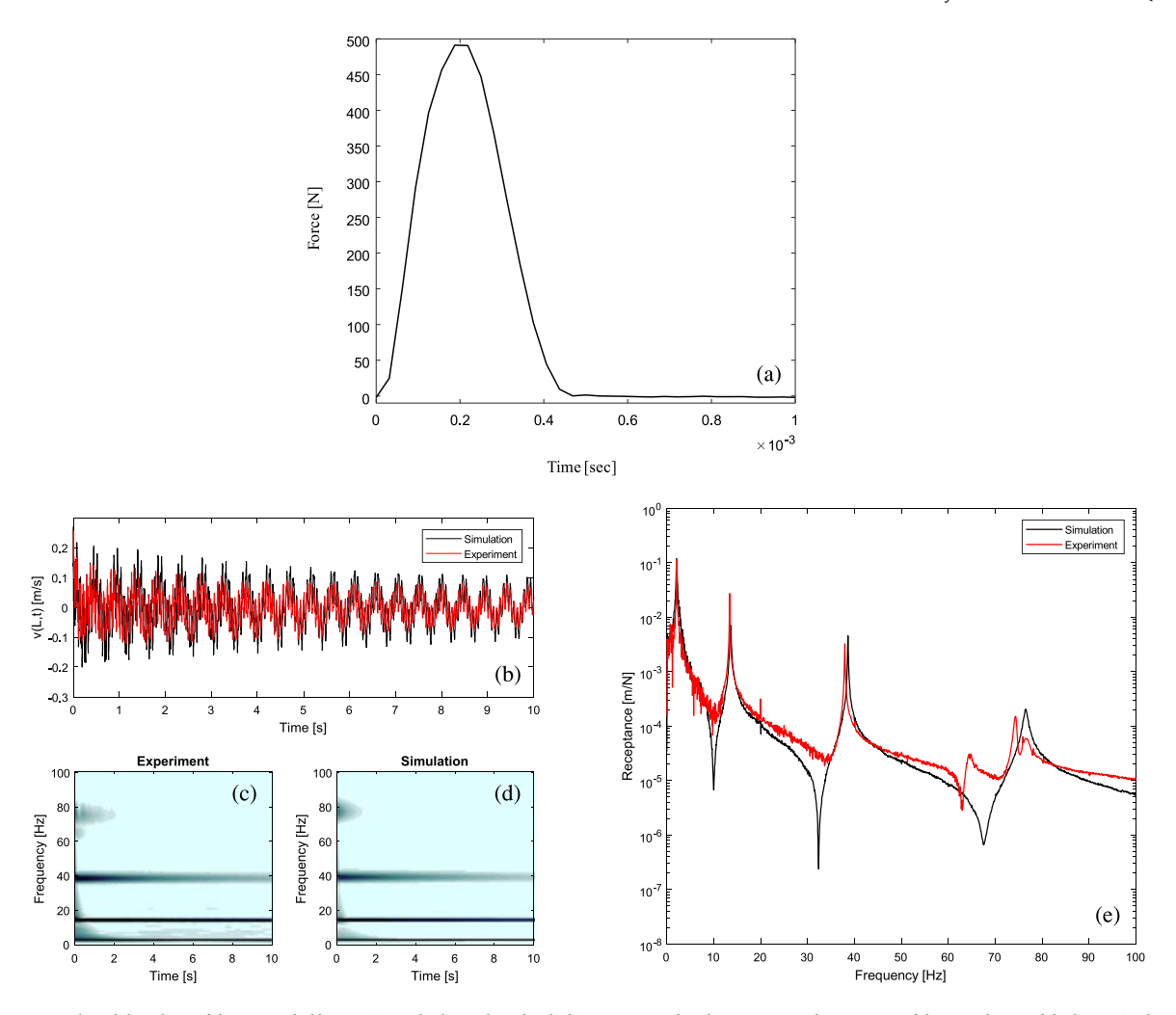


Fig. 14. Experimental modal analysis of the uncoupled beam: (a) Applied impulsive load, (b) experimental and computational time series of the tip velocity of the beam, (c, d) experimental and computational wavelet spectra of the shown velocity time series, and (e) corresponding experimental and computational direct receptance frequency response functions.

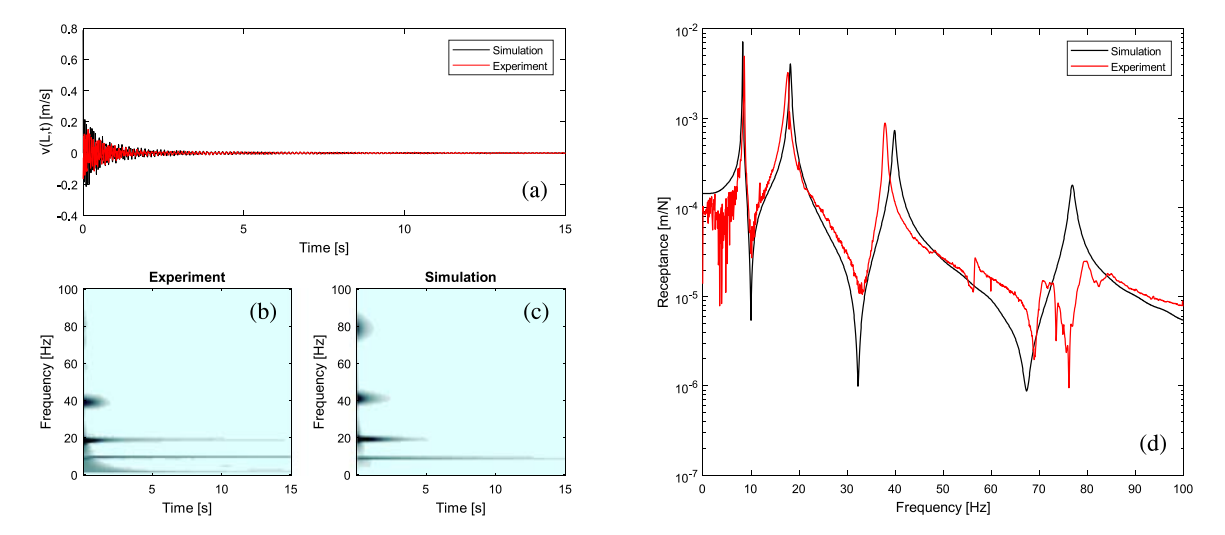


Fig. 15. Experimental modal analysis of the coupled beam: (a) Experimental and computational time series of the tip velocity of the beam, (b, c) experimental and computational wavelet spectra of the shown velocity time series, and (d) corresponding experimental and computational direct receptance frequency response functions.

intrinsic mode functions (IMFs) [26–28]. WBEMD is a closed-loop, optimization-based method for post-processing measured oscillating time series, yielding the dominant embedded component oscillations that are governed by different time scales. Hence, WBEMD is a numerical method to compute the different oscillating processes (the IMFs) and the

corresponding governing time scales (or frequencies) that are embedded in the oscillating time series. The superposition of all identified IMFs reconstructs the measured signal, and the dominant (i.e., the first) IMF reveals the dominant time scale (or frequency) that governs the oscillating signal. In our case the first IMF of each velocity time series is

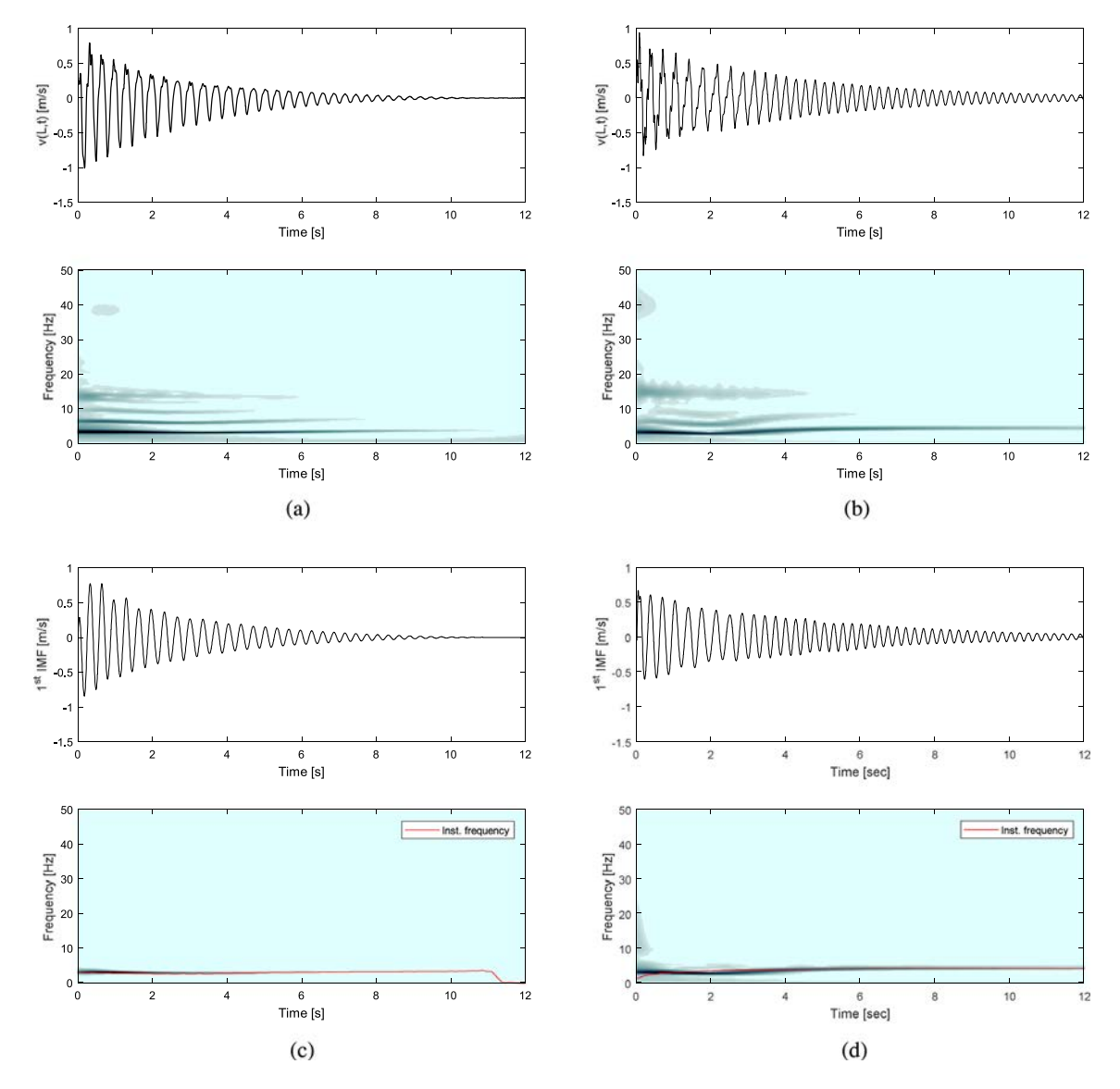


Fig. 16. Comparison between experimental and computational results for initial angle of inclination, $\phi_0 = 20^\circ$ and initial tip displacement, $u_0 = -0.06$ m: (a) Experimental tip velocity and associated wavelet spectrum; leading order experimental (c) and computational IMF, and associated wavelet spectrum (red lines in (c) and (d) indicate instantaneous frequency of the IMFs.

at the frequency of the first bending mode of the beam and confirms that it is that mode that dominates the nonlinear response; in essence, the time series of the first IMF of each velocity time series that is depicted in Figs. 15–17 represents the response of the first bending mode of the coupled beam.

As expected from the previous theoretical analysis with the SDOF model of Fig. 1, the geometric nonlinearity induces both hardening and softening behavior. Indeed, it is clear from the results of Fig. 17 that the frequency of the first bending mode and its higher harmonics are initially decreasing with decreasing energy (indicating hardening nonlinearity) until 3.3 s. After 3.3 s, however, the behavior of the nonlinearity switches from hardening to softening nonlinearity with the frequency increasing with decreasing energy. Higher bending modes are almost not affected by the geometric nonlinearity. Similar trends are noted for the other responses depicted in Figs. 16 and 18.

Moreover, comparing the experimental and computational timeseries and their associated wavelets in Figs. 16–18, we conclude that the FE model can accurately model the dynamics of the experimental coupled beam. In particular, the computational time series appears to capture accurately the high frequency nonlinear scattering of energy observed in the experiments, as well as the hardening/softening behavior of the coupled system as evidenced in the dominant IMFs and

Table 5
Logarithmic decays for the first IMFs of the experimental and computational velocity time series.

Initial Disp. [m]	$ au_{NL}(\phi_0)$ - Experiment		[m] $ au_{NL}(\phi_0)$ - Experiment $ au_{NL}(\phi_0)$	$ au_{NL}(\phi_0)$ - Sin	$_{\mathrm{N}L}(\phi_0)$ - Simulation	
	$\phi_0 = 16.5^{\circ}$	$\phi_0 = 20^\circ$	$\phi_0 = 16.5^{\circ}$	$\phi_0 = 20^\circ$		
0.037	6.1023	4.8804	15.5262	10.7852		
0.050	7.9840	5.9739	16.3504	11.6186		
0.055	8.6301	6.3481	16.9023	11.7009		
0.060	11.2021	8.1016	18.1719	12.8816		

their wavelet transforms. However, since friction in the hinges of the inclined element is not modeled in the FE model, the response of the FE model appears to be more lightly damped, persisting longer than that of the experiment. This affects the later rather than the earlier transient response of the coupled beam. It is clear from these results that primarily the first bending mode is affected by the geometric nonlinearity. Moreover, one can clearly see the hardening behavior along with the higher harmonics of the first mode. This hardening behavior confirms our previous observations in the SDOF system and show that the nonlinearity behaves the same way in this case as well.

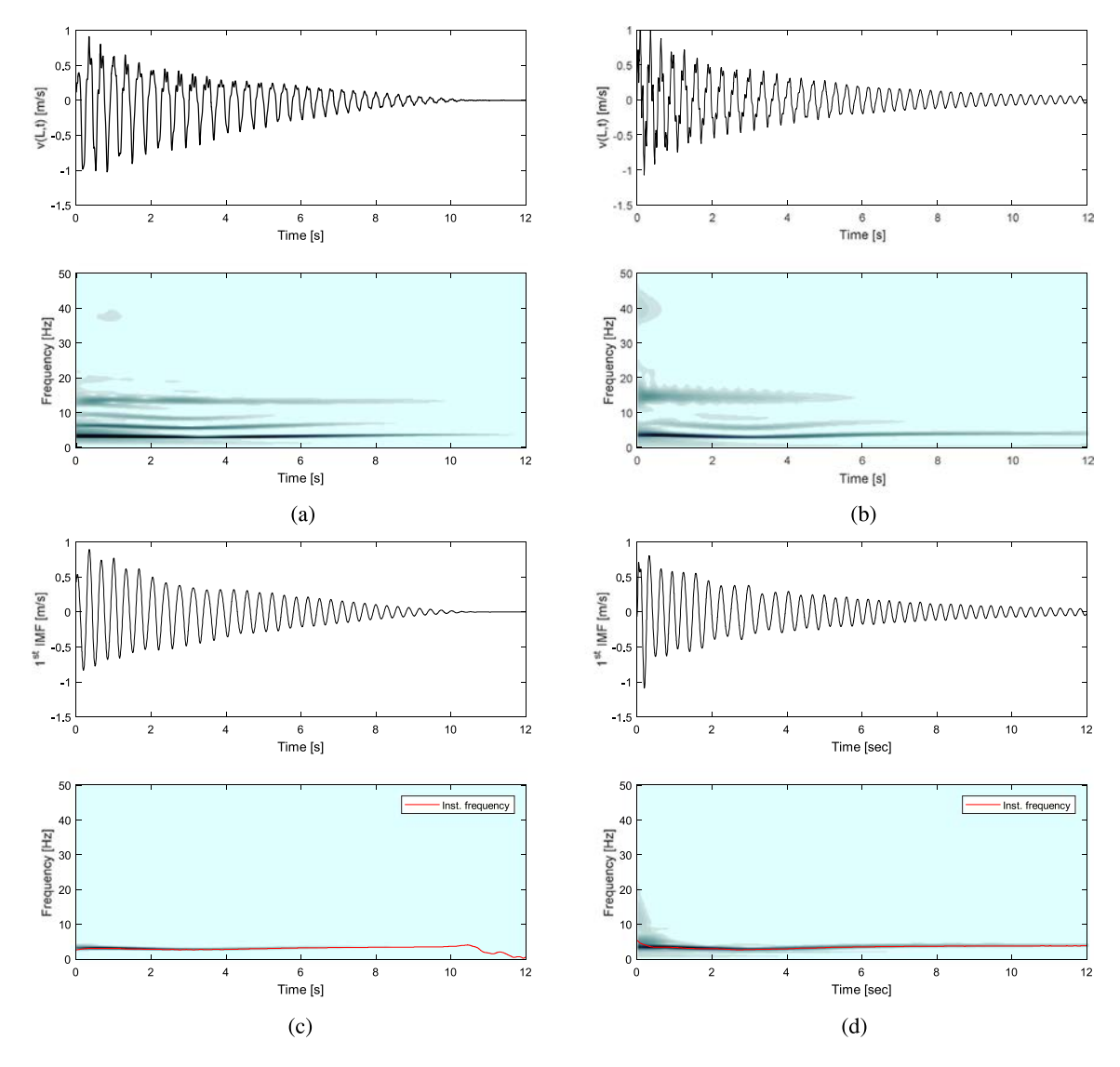


Fig. 17. Comparison between experimental and computational results for initial angle of inclination $\phi_0 = 16.5^{\circ}$ and initial tip displacement $u_0 = -0.06 \,\mathrm{m}$: (a) Experimental tip velocity and associated wavelet spectrum; leading order experimental (c) and computational IMF, and associated wavelet spectrum (red lines in (c) and (d) indicate instantaneous frequency of the IMFs.

To validate the effect of the initial angle on the time-scale of the slow-dynamics of the damped dynamics and verify the theoretical predictions, the main harmonic consisting of the first bending mode response was computed by WBEMD and examined further. This enables us to have a fairer comparison between the theoretical prediction from the SDOF system of Fig. 1 and the experimental results with the coupled beam of Fig. 13, which is a continuous elastic system. Hence, only the dominant first IMF of each experimental measurement was considered in the following study. To this end, the decay time constant as defined in the theoretical section can be determined by computing the instantaneous amplitude of the first IMF, using the Hilbert transform. Experiments were performed for four different initial tip displacements, namely -0.06 m, -0.055 m, -0.05 m, -0.037 m, and two different initial angles of inclination, that is, $\phi_0 = 16.5^\circ$ and $\phi_0 = 20^\circ$. Along with each experimental measurement, a similar post-processing analysis was performed for the corresponding computational times series. The results are listed in Table 5.

Fig. 19(a) illustrates the comparison between the ratios of velocity logarithmic decays – each computed by relation (13) – for the two initial angles of inclination considered in Table 5, both for the experimental measurements and the computational simulations. As inferred from theoretical relations (14) and (15), the predicted ratio of logarithmic

decays should not depend on the initial energy of the oscillation (i.e., the initial amplitude). Yet, in the experimental system and its corresponding numerical model, due to the existence of higher flexible modes and other unmodeled effects (e.g., friction at the pinned joints of the attachment, and noise in the measurements), the percentage of the input energy that applies to the first bending mode (the first IMF) is different for different initial displacements. Hence, the ratios of logarithmic decays for the coupled beam do vary for different initial displacements. However, there is satisfactory agreement between the predicted values and the experimental and computational ones for the coupled beam, especially at higher initial tip displacements (energies). This might be explained by the fact that at higher energies the geometric nonlinearities are expected to be more profound and to dominate the transient response compared to the underlying linear dynamics. In fact, as the initial displacement decreases, the effect of friction becomes more dominant compared to the effect of viscous damping in the system, and so the errors compared to the theoretical prediction increase. In addition, at higher amplitudes of the oscillations the effect of noise and unmodeled effects on the results appear to decrease. Fig. 19(b) depicts the errors of the experimental and computational ratios compared to the theoretical prediction.

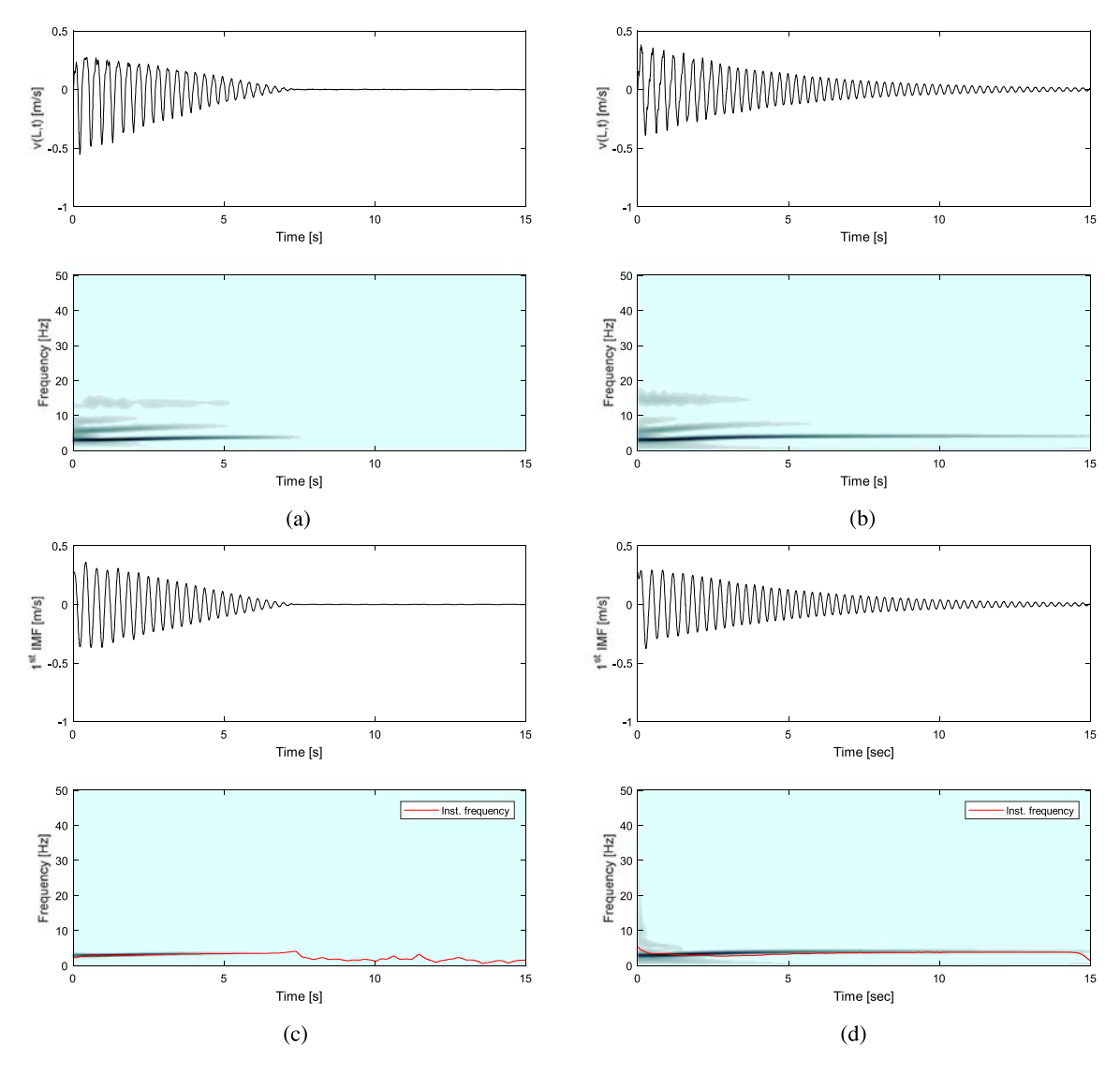


Fig. 18. Comparison between experimental and computational results for initial angle of inclination $\phi_0 = 16.5^{\circ}$ and initial tip displacement $u_0 = -0.05 \,\mathrm{m}$: (a) Experimental tip velocity and associated wavelet spectrum; leading order experimental (c) and computational (d) IMF, and associated wavelet spectrum (red lines in (c) and (d) indicate instantaneous frequency of the IMFs.

6. Concluding remarks

In this work a new way to induce geometrically nonlinear stiffness and damping nonlinearities in a system composed of otherwise linear elements was studied. The study contained analytical, computational and experimental parts. In the theoretical study a SDOF oscillator was considered, consisting of a mass restricted to oscillate in the vertical direction and grounded by a linear spring and a linear damper and two parallel spring—dashpot elements which while at rest, create in initial inclination angle with the ground. When at equilibrium all stiffness and damping elements of this system are assumed to be uncompressed, so no gravity forces are included in the analysis. The mass is forced with an initial impulse of varying intensity.

In the theoretical part it was shown that the initial angle of inclination can cause two bifurcations in the transient damped dynamics of the system. The first bifurcation corresponds to the initial angle after which the system experiences negative stiffness in its restoring force. The second bifurcation corresponds to the initial angle after which the number of equilibrium points in the system changes from being one to three, two of which are stable and one is unstable. Moreover, it was shown that for zero initial angle, the stiffness nonlinearity is purely hardening, while for any non-zero initial angle, and depending

in the input energy to the system, the nonlinearity can either change its behavior from hardening (in the initial high energy regime) to softening (in the later lower energy regime), or to only softening behavior (at sufficiently low input energy). In addition, the linearized natural frequency that the system eventually attains at the end of the low-energy softening response was shown to be tunable with the initial angle of the inclined elements.

In the numerical simulations it was observed that by changing the initial inclination angle one can affect the time-scale of the slow-dynamics of the transient decay of the impulsive response, and at that low-energy regime the effect of the geometrically nonlinear damping on the dynamics was analytically investigated. Using the complexification-averaging (CX-A) method the slow-flow equation governing the slow-dynamics of the decaying response was derived and solved exactly. The numerical observations then were verified by the results obtained from the CX-A method.

In the experimental part of this work, a validation of the theoretical predictions was sought. To this end, a series of experimental tests was undertaken with a beam which was clamped at one end and grounded through an inclined dissipative spring element. Furthermore, a numerical FE model of the experiment was constructed to be able to predict the behavior of the system and further verify the

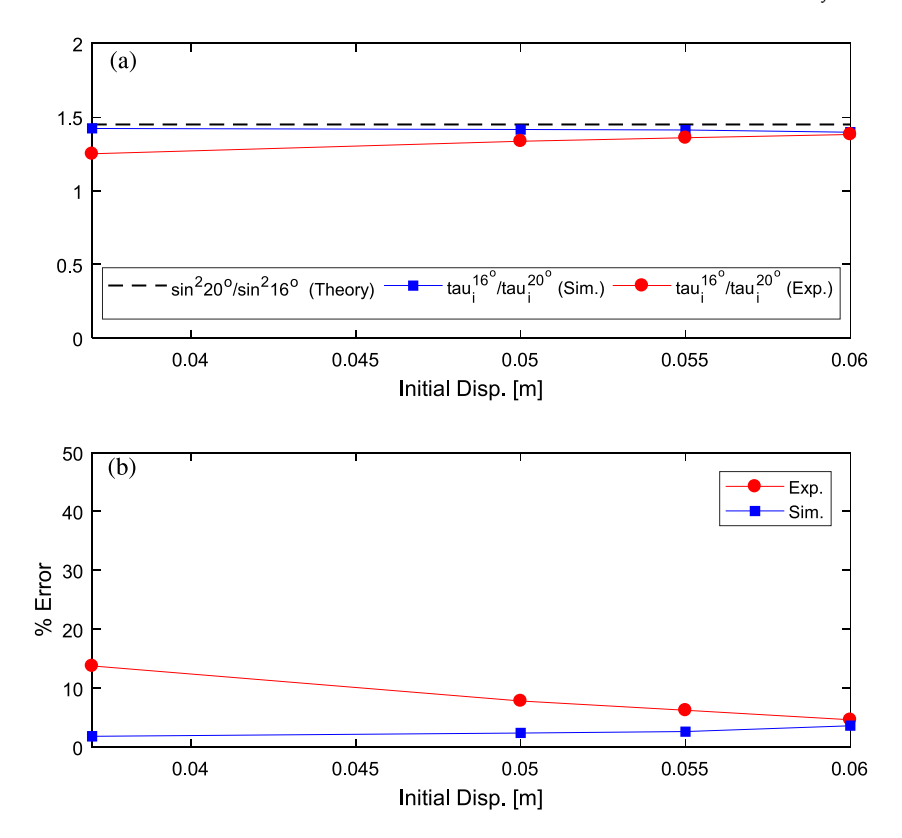


Fig. 19. Ratios of the velocity logarithmic decays referring to the data of Table 5: (a) Experimental (red line) and computational (blue line) ratio $\tau_{NL}(16.5^{\circ})/\tau_{NL}(20^{\circ})$ for different initial amplitudes compared with the theoretical value $\sin^2(20^{\circ})/\sin^2(16.5^{\circ})$ (dashed line); (b) Percent error with respect to the theoretical prediction. (For interpretation of the references to color in this figure legend, the reader is referred to the web version of this article.)

theoretical results. The gathered data from the experiment and their corresponding numerical simulations with the FE model validated the theoretical results and the numerical observations which were derived based on the theoretical SDOF model. The fact that we observed the same types of experimental nonlinear behaviors to those predicted with the theoretical discrete model, confirmed the robustness of the geometrically nonlinear effects induced by the inclined spring–damper elements.

The results reported in this work underscore the need to carefully evaluate the effects of geometry and kinematics on the responses of discrete or continuous oscillators, since strong hardening–softening stiffness and damping nonlinearities may result in certain frequency and energy ranges, despite the fact that these systems may consist of stiffness and damping elements with linear constitutive laws.

Acknowledgments

This work was supported in part by National Science Foundation, United States, Grant No. CMMI-17-1727761, and by the National Science Foundation Graduate Research Fellowship DGE-1144245 (Keegan Moore). Any opinion, findings, and conclusions or recommendations expressed in this work are those of the authors and do not necessarily reflect the views of the National Science Foundation.

Appendix. Taylor series expansions of the nonlinear stiffness and damping forces

The leading order coefficients of the Taylor series expansions of the nonlinear stiffness force in the approximate system (6) are given by,

$$\begin{split} C_0 &= \frac{1}{2} \sin^2 \phi_0 \tan \phi_0, \\ C_1 &= -\frac{1}{128} \tan \phi_0 \cos^2 \phi_0 \left(128 - 192 \cos^2 \phi_0\right) + \frac{1}{2} \sin^2 \phi_0, \\ C_2 &= \frac{1}{128} \tan \phi_0 \cos^3 \phi_0 \sin \phi_0 \left(128 - 320 \cos^2 \phi_0\right) \\ &- \frac{1}{128} \cos^2 \phi_0 \left(128 - 192 \cos^2 \phi_0\right), \\ C_3 &= -\frac{1}{128} \tan \phi_0 \cos^4 \phi_0 \left(128 - 640 \cos^2 \phi_0 + 560 \cos^4 \phi_0\right) + \\ &+ \frac{1}{128} \cos^3 \phi_0 \sin \phi_0 \left(128 - 320 \cos^2 \phi_0\right), \\ C_4 &= \frac{1}{128} \tan \phi_0 \cos^5 \phi_0 \sin \phi_0 \left(128 - 896 \cos^2 \phi_0 + 1008 \cos^4 \phi_0\right) - \\ &- \frac{1}{128} \cos^4 \phi_0 \left(128 - 640 \cos^2 \phi_0 + 560 \cos^4 \phi_0\right), \\ C_5 &= \frac{1}{128} \cos^5 \phi_0 \sin \phi \left(128 - 896 \cos^2 \phi_0 + 1008 \cos^4 \phi_0\right), \end{split}$$

$$(A.1)$$

where ϕ_0 denotes the initial angle of inclination. Similarly, the corresponding leading-order Taylor-series coefficients for the nonlinear damping force are given by:

$$D_{0} = \frac{1}{2} \left(1 - \cos^{2} \phi_{0} \right),$$

$$D_{1} = \frac{1}{4} \left(\sin^{4} \phi_{0} + 2 \sin^{2} \phi_{0} \right),$$

$$D_{2} = \frac{1}{8} \left(\cos^{6} \phi_{0} + 3 \cos^{4} \phi_{0} + 3 \cos^{2} \phi_{0} + 1 \right),$$

$$D_{3} = -\frac{1}{16} \left(\sin^{8} \phi_{0} + 4 \sin^{6} \phi_{0} + 6 \sin^{4} \phi_{0} + 4 \sin^{2} \phi_{0} \right),$$

$$D_{4} = -\frac{1}{32} \left(\cos 10\phi_{0} + 5 \cos^{8} \phi_{0} + 10 \cos^{6} \phi_{0} + 10 \cos^{4} \phi_{0} + 5 \cos^{2} \phi_{0} + 1 \right),$$

$$D_{5} = \frac{1}{64} \left(\sin^{12} \phi_{0} + 6 \sin^{10} \phi_{0} + 15 \sin^{8} \phi_{0} + 20 \sin^{6} \phi_{0} + 15 \sin^{4} \phi_{0} + 6 \sin^{2} \phi_{0} \right),$$
(A.2)

Hence, these coefficients depend only on the initial angle of inclination and on no other system parameter.

References

- A.M. Reinhorn, S. Viti, G. Cimellaro, Proceedings of the 37th UJNR Panel Meeting on Wind and Seismic Effects, 2005, pp. 16–21.
- [2] S. Viti, G.P. Cimellaro, A.M. Reinhorn, Retrofit of a hospital through strength reduction and enhanced damping, Smart Struct. Syst. 2 (2006) 339–355.
- [3] M.J. Brennan, Vibration control using a tunable vibration neutralizer, Proc. Inst. Mech. Eng. C 211 (1997) 91–108.
- [4] M.J. Brennan, Some recent developments in adaptive tuned vibration absorbers/neutralisers, Shock Vib. 13 (2006) 531–543.
- [5] O. El-Khoury, H. Adeli, Recent advances on vibration control of structures under dynamic loading, Arch. Comput. Methods Eng. 20 (2013) 353–360.
- [6] B. Philip, J.B. Michael, J.E. Stephen, Vibration control using an adaptive tuned vibration absorber with a variable curvature stiffness element, Smart Mater. Struct. 14 (1055) (2005).
- [7] D.J. Thompson, A continuous damped vibration absorber to reduce broad-band wave propagation in beams, J. Sound Vib. 311 (2008) 824–842.
- [8] A. Unal, Y. Arcan, B. Mehmet, Control of structural response under earthquake excitation, Comput.-Aid. Civ. Infrastruct. Eng. 27 (2012) 620–638.
- [9] F. Georgiades, A.F. Vakakis, Dynamics of a linear beam with an attached local nonlinear energy sink, Commun. Nonlinear Sci. Numer. Simul. 12 (2007) 643–651.
- [10] C.-H. Lamarque, O.V. Gendelman, A. Ture Savadkoohi, E. Etcheverria, Targeted energy transfer in mechanical systems by means of non-smooth nonlinear energy sink, Acta Mech. 221 (175) (2011).
- [11] Y. Starosvetsky, O.V. Gendelman, Vibration absorption in systems with a nonlinear energy sink: Nonlinear damping, J. Sound Vib. 324 (2009) 916–939.
- [12] A.F. Vakakis, O.V. Gendelman, L.A. Bergman, D.M. McFarland, G. Kerschen, Y.S. Lee, Nonlinear Targeted Energy Transfer in Mechanical and Structural Systems, Springer, Netherlands, 2008.
- [13] I.A. Antoniadis, D.T. Venetsanos, F.G. Papaspyridis, Dynamic non-linear energy absorbers based on properly stretched in-plane elastomer structures, Nonlinear Dynam. 75 (2014) 367–386.
- [14] A. Carrella, M.J. Brennan, T.P. Waters, Static analysis of a passive vibration isolator with quasi-zero-stiffness characteristic, J. Sound Vib. 301 (2007) 678–689.
- [15] B.A. Fulcher, D.W. Shahan, M.R. Haberman, C. Conner Seepersad, P.S. Wilson, Analytical and experimental investigation of buckled beams as negative stiffness elements for passive vibration and shock isolation systems, J. Vib. Acoust. 136 (2014) 031009.

- [16] F. Liu, X. Pang, Z. Liu, T. Zhang, H. Huang, J. Zhu, 2010 3rd International Nanoelectronics Conference, INEC, 2010, pp. 154–155.
- [17] D.L. Platus, SPIE's international symposium on optical science, Eng. Instrum. SPIE 3786 (8) (1999).
- [18] W. Wu, X. Chen, Y. Shan, Analysis and experiment of a vibration isolator using a novel magnetic spring with negative stiffness, J. Sound Vib. 333 (2014) 2958–2970.
- [19] A. Carrella, M.J. Brennan, T.P. Waters, Optimization of a quasi-zero-stiffness isolator, J. Mech. Sci. Technol. 21 (946) (2007).
- [20] A.A. Sarlis, D.T.R. Pasala, M.C. Constantinou, A.M. Reinhorn, S. Nagarajaiah, D. Taylor, COMPDYN 2011, Proc. of 3rd ECCOMAS Thematic Conference on Computational Methods in Structural Dynamics and Earthquake Engineering, Corfu, Greece. 2011.
- [21] A. Carrella, M.J. Brennan, T.P. Waters, V. Lopes, Force and displacement transmissibility of a nonlinear isolator with high-static-low-dynamic-stiffness, Int. J. Mech. Sci. 55 (2012) 22–29.
- [22] D. Andersen, Y. Starosvetsky, A. Vakakis, L. Bergman, Dynamic instabilities in coupled oscillators induced by geometrically nonlinear damping, Nonlinear Dynam. 67 (2012) 807–827.
- [23] H. Cho, B. Jeong, M.-F. Yu, A.F. Vakakis, D.M. McFarland, L.A. Bergman, Nonlinear hardening and softening resonances in micromechanical cantilever-nanotube systems originated from nanoscale geometric nonlinearities, Int. J. Solids Struct. 49 (2012) 2059–2065.
- [24] K. Asadi, J. Li, S. Peshin, J. Yeom, H. Cho, Mechanism of geometric nonlinearity in a nonprismatic and heterogeneous microbeam resonator, Phys. Rev. B 96 (2017) 115306.
- [25] M.H. Richardson, D.L. Formenti, Proceedings of the Third International Modal Analysis Conference, 1985, pp. 390–397.
- [26] K.J. Moore, M. Kurt, M. Eriten, D.M. McFarland, L.A. Bergman, A.F. Vakakis, Wavelet-bounded empirical mode decomposition for vibro-impact analysis, Nonlinear Dynam. 93 (2018) 1559–1577.
- [27] K.J. Moore, M. Kurt, M. Eriten, D.M. McFarland, L.A. Bergman, A.F. Vakakis, Wavelet-bounded empirical mode decomposition for measured time series analysis, Mech. Syst. Signal Process. 99 (2018) 14–29.
- [28] Y.S. Lee, S. Tsakirtzis, A.F. Vakakis, D.M. McFarland, L.A. Bergman, Physics-based foundation for empirical mode decomposition: Correspondence between intrinsic mode functions and slow flows, AIAA J. 47 (2938) (2009) 12–2963.